Pathway to Complete Energy Sector Decarbonization with Available Iridium Resources Using Ultra-Low Loaded Water Electrolyzers

Zachary Taie[1,2], Xiong Peng[1*], Devashish Kulkarni[4], Iryna V. Zenyuk[3,4], Adam Weber[1], Christopher Hagen[2], Nemanja Danilovic[1*]

[1] *Lawrence Berkeley National Laboratory, Energy Technologies Area, Energy Conversion Group, Berkeley, California 94720, USA*

[2] *Oregon State University, School of Mechanical, Industrial, and Manufacturing Engineering, Bend, OR 97702, U.S.*

[3] *University of California Irvine, National Fuel Cell Research Center, Department of Chemical Biomolecular Engineering;* [4]*Department of Material Science and Engineering, Irvine, California 92697, USA*

[*] Corresponding authors: xiongp@lbl.gov, ndanilovic@lbl.gov

Abstract

We present ultra-low Ir loaded (ULL) proton exchange membrane water electrolyzer (PEMWE) cells that can produce enough hydrogen to largely decarbonize the global natural gas, transportation, and electrical storage sectors by 2050, using only half of the annual global Ir production for PEMWE deployment. This represents a significant improvement in PEMWE's global potential, enabled by careful control of the anode catalyst layer (CL), including its mesostructure and catalyst dispersion. Using commercially relevant membranes (Nafion™ 117), cell materials, electrocatalysts and fabrication techniques, we achieve at peak a 250x improvement in Ir mass activity over commercial PEMWEs. An optimal Ir loading of 0.011 mg_{Ir} cm^{-2} operated at an Ir-specific power of ~100 MW kg_{Ir}^{-1} at a cell potential of ~1.66 V vs. RHE (85% higher heating value efficiency). We further evaluate the performance limitations within the ULL regime and offer new insights and guidance in CL design relevant to the broader energy conversion field.

Keywords: hydrogen, electrolysis, PEMWE, ultra-low loading, iridium, overpotential analysis

Introduction

Diffusing marginally low-cost renewable electricity into sectors that heavily rely on fossil fuels present a major global challenge in fully decarbonizing our energy system. Renewably generated electricity is now cost competitive with fossil-derived sources, even when excluding subsidies[1], and accounted for nearly 45% of newly installed global electrical generation capacity in 2018[2]. Conversely, renewable energy served less than a quarter of new energy demand growth during that same year. One approach to increase the penetration of this low-carbon energy is to fully electrify all sectors, which shows promise for some, such as light duty transportation[3], short-term electricity storage[4], and space heating[5]. However, over a quarter of global CO_2 emissions originate from industries that are difficult to decarbonize through direct electrification, such as aviation, heavy-duty transportation, long-term energy storage, and steel and cement production[6]. These sectors require a renewable energy carrier with properties similar to fossil-derived hydrocarbon fuels. "Green" hydrogen, i.e. hydrogen produced via water electrolysis using renewable electricity, and renewable hydrocarbon fuels synthesized from green hydrogen and captured carbon, present the most promising paths towards decarbonizing these sectors[7–9]. In each case a highly efficient and scalable electrolysis technology is urgently needed to supply the base green hydrogen feedstock.

Proton exchange membrane (PEM) water electrolysis (PEMWEs) is gaining popularity amongst available electrolysis chemistries due to its small footprint, high turn-down ratio, pressurized hydrogen delivery, and quick start-up and response times[10]. Further, its advanced technical maturity over developing chemistries, such as anion exchange membrane (AEM) electrolysis, provides the highest probability of global-scale adoption within the next three decades, a time horizon understood to provide a greater than 50% chance of keeping global temperature from rising 2 °C above pre-industrial levels[11]. Though high hydrogen production costs have historically limited PEMWE adoption, production costs of < \$4 kg_{H2}^{-1} (1 \$ kg_{H2}^{-1} approximately equals 1 \$ gallon of gasoline equivalent^{-1}) can now be realized in 20 U.S. states

using existing utility tariff structures, including a very competitive lower bound of \$2.60 kg_{H2}^{-1} [12]. Declining renewable electricity rates have primarily driven this cost reduction since the majority of total hydrogen production cost is derived from the electrical feedstock itself[13,14]. As the cost of hydrogen becomes competitive in select markets, initial industrial interest is arriving at a scale of multi-to-hundreds of MW per instillation[15,16]. At this scale commercial PEMWEs are scarce and the economic and deployment challenges are dissimilar from the more familiar kW scale. Specifically, two challenges unique to the MW regime have arisen: (1) catalyst cost becomes a significant fraction of the overall capital cost at the MW scale[17]; and (2) there are severe global supply restrictions on iridium (Ir), the only anodic oxygen evolution reaction (OER) electrocatalyst that has shown the required combination of activity and durability necessary for commercial applications. The economic challenge is straightforward: reducing the Ir and Pt loading in the devices will decrease the overall capital cost, thereby decreasing hydrogen production cost. Timely cost reduction is critical to maintain the PEMWE adoption momentum that has accumulated, especially at this important pilot-scale deployment juncture. Catalyst loading reduction is even more critical when considering the limited Ir reserves. Ir is the least abundant element on earth, with a global annual production of only 7.25 tonnes, mainly from South Africa[18], Zimbabwe[19], Canada[20], Russia, and the United States[21]. To realize meaningful adoption past the pilot scale level, we must better utilize this limited supply. Current commercial electrolyzers have an Ir-specific power (a figure of merit for catalyst utilization), p [MW kg_{ir}^{-1}], defined as

$$p = \frac{i * HHV}{2F * l} * 1000 \left[\frac{\frac{MW}{kg}}{\frac{kW}{mg}} \right] \qquad \textit{Equation 1}$$

where i is the operating current density [A cm^{-2}], HHV is the higher heating value of hydrogen (285,796 kJ $kmol^{-1}$), F is faradays constant (96.5 E^6 coulomb $kmol^{-1}$), l is the anode Ir loading [mg_{Ir} cm^{-2}] (the final term is a unit conversion), of ~2 MW kg_{Ir}^{-1} [22] when measuring the current density at a higher heating value (HHV) based efficiency of 88% (1.6 V vs reversible hydrogen electrode (RHE), chosen to limit wasted electrical feedstock). If half of the global Ir supply, 3.6 t a^{-1}, was used for PEMWE deployment the feasible annual PEMWE deployment would thus currently be 7.2 GW a^{-1}. Given the world has an annually-averaged fossil fuel power

consumption of ~15 TW[23] this would be an insignificant level of penetration. Ir utilization must be increased if PEMWEs are to play a significant role in decarbonization from both a hydrogen production cost and resource availability perspective. We reserve detailed deployment targets for the discussion section alongside our approach to enabling increased Ir utilization.

In this study we demonstrate PEMWE cells that would enable the production of enough hydrogen to satisfy the global transportation, long-term electricity storage, and natural gas demand by 2050 using only half of the annual global Ir availability. We accomplish this by tailoring the mesoscale interfaces in the anode catalyst layer (CL) to increase catalyst utilization and improve performance over commercial MEAs, while reducing the Ir loading to ultra-low loading (ULL) levels. First, X-ray fluorescence (XRF) mapping, scanning electron microscopy (SEM), and micro X-ray computed tomographic (XCT) reconstructions of the ULL anode CL, and CL-porous transport layer (PTL) interface are used to produce exceptional ULL CLs and PTL-CL interfaces. Then, novel polarization performance and activation, ohmic, and mass transport overpotentials at ultra-low Ir loadings, thus-far unreported, are presented and discussed. Finally, the global deployment and decarbonization impacts of the evolved ULL regime is analyzed, proving that even with limited Ir resources PEMWEs can play a significant role in decarbonizing the global energy system.

Results and discussion

Initial ULL PEMWE studies have shown poor performance relative to high-loaded baseline cells[17,24–26], which has led to an understanding that new electrocatalyst or porous transport layers are necessary to realize baseline performance at low loading. We hypothesize these conclusions likely derive from suboptimal catalyst layers which suffer from poor catalyst utilization[27]. These inadequate catalyst layers have contributed to the belief that ULL PEMWEs have inherent performance limitations that preclude the ULL regime from commercial relevance and imposes a ceiling on the global impact of PEMWEs due to Ir resource limitations[10,17,28,29]. A popular approach to combat this limitation is supporting Ir nanoparticles on conductive materials which maximizes Ir surface area to volume ratio and utilizes the Ir more effectively while

reducing CL cost. The support particle size can also be optimized for easier ink processing and can allow for a tailorable or constant CL thickness as Ir loading is reduced. However, supported catalysts have not shown performance equal to commercial IrO_x catalysts. Often, the poor ULL performance and limited Ir resources is used as an argument for the alkaline electrolysis routes which can utilize non-precious metals, but currently lack the performance or durability to fulfill the imminent need. Thus, we set out to find the true performance limitation of ULL PEMWE by using a rational design approach of the ULL anode CL which required extensive attention to the CL mesostructure and electrified interfaces.

ULL PEMWE Performance

We were able to significantly improve performance relative to higher loaded commercial CCMs at Ir loading reductions of 15 to 96 fold, and also maintain commercial performance at an Ir loading reduction of 227 fold, Figure 1. At 2 A cm^{-2} we recorded an overpotential reduction between 104 and 33 mV at Ir loadings of 0.17 and 0.026 mg_{Ir} cm^{-2} (Ir loading reduction of 15-96 fold), respectively, while also matching commercial performance at 1.4 A cm^{-2} at an Ir loading of 0.011 mg_{Ir} cm^{-2} (Ir loading reduction of 227 fold). This represents an impressive improvement in ULL performance that was accomplished solely by improving the catalyst distribution and mesoscale structure of the anode CL, as discussed below, while using unmodified commercial PTLs. Though literature consensus seems to suggest that PTL modifications are necessary to improve the PTL CL interface[10,30,31], and thus cell performance, these result suggest that the CL side of the interface plays a larger role than previously believed. We reserve detailed discussion of the implications of this interfacial improvement for later sections and will first discuss the efforts that went into producing the high-quality anode CLs.

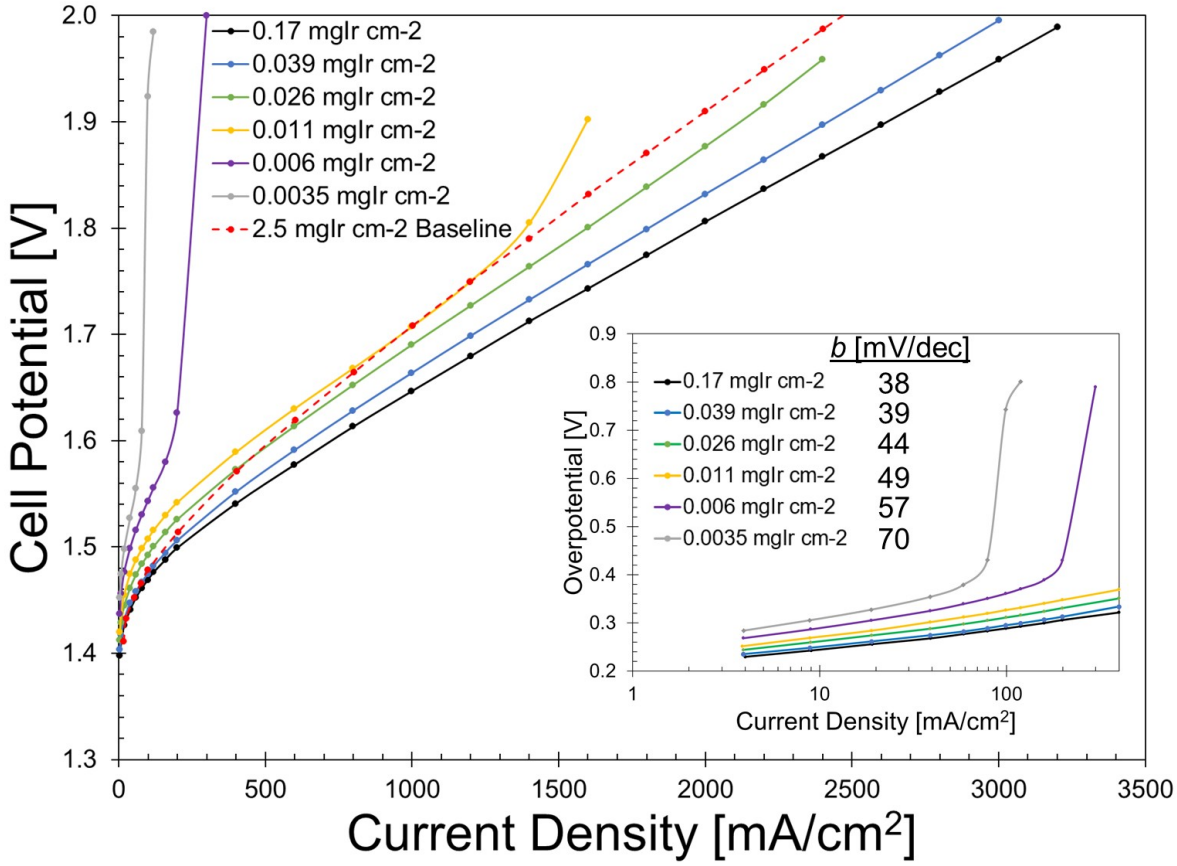

Figure 1. PEMWE polarization curves at different Ir loadings at an optimal ionomer/catalyst ratio of 0.116. Loadings are reported as iridium metal cm^{-2}, measured using XRF. Inset shows Tafel plot using current density [mA cm^{-2}] (the area is the cell active area – 5 cm^2), as the reaction rate coordinate with calculated Tafel slopes, b, listed. Cathode Pt loadings were kept at 0.2 ± 0.02 mg_{Pt} cm^{-2} for all tests. Testing was conducted at 80 °C with a Nafion™ 117 membrane. The red dashed line represents baseline performance of a commercial 2.5 mg_{Ir} cm^{-2} loaded MEA (Greenerity E400) round-robin tested at 5 independent laboratories for the IEA Electrolysis Annex 30[32].

Rational catalyst layer design and morphology

We use ultrasonic spray coating to fabricate the ULL CLs as it provides unprecedented control of the CL formation during fabrication, which is necessary for R&D work. While this may not be a scalable technique at high Ir loadings due to the long spray time required, the spray time in the ULL regime is greatly reduced making this a feasible technique for scale-up. First, significant effort was committed to optimizing the spraying process and ink recipe to ensure a well-distributed, homogenous, porous CL at each loading. Homogeneous and unbroken coverage

is probably the single most important factor in maximizing performance at ULL because it provides continuous electrical percolation networks which are critical for high catalyst utilization[33–35], while also providing integral contact between the CL and porous transport layer (PTL), maximizing electronically accessible triple phase boundary area and reducing interfacial and CL electronic resistance. We used several physical characterization techniques to guide the fabrication evolution including scanning electron microscopy (SEM), X-ray fluorescence (XRF) mapping, and micro-X-ray computed tomography (XCT).

We first used dynamic light scattering (DLS) to enhance the stability of the Ir based ink used for spray deposition by varying the solvent composition until a stable ink was found (Figure S1 and S2). Ink stability is crucial so the Ir particles do not precipitate out of the solution in the syringe or in the feed line, which would hinder even distribution of Ir in the active area. The inks used in the study were particularly dilute, with solids loading below 0.1%, which allowed for slower layer-by-layer buildup than higher concentration spray coating approaches. Tens of spray passes were required even when fabricating ULL anode CLs, which allowed for the ink and the resulting catalyst aggregates to distribute evenly through the active area, resulting in more distributed catalyst instead of large local agglomerations as is common with higher concentration inks. For comparison, XRF maps of the lowest Ir loaded ULL regime anode (using a dilute ink – 0.08% solids) and a typical Pt cathode (using a more concentrated ink – 0.27% solids) are compared in Figure 2 to better understand the effects of dilute ink fabrication. The locally high Pt concentrations in Figure 2 b) are not visible by eye, or readily apparent using SEM, but greatly limit the effective CL geometric area due to catalyst-sparse regions. The heterogeneity of the cathode catalyst layer is of little consequence for two concomitant reasons: the fast kinetics of the hydrogen evolution reaction on Pt, and the use of Pt *supported on carbon* as a catalyst results in relatively thicker catalyst layers with adequate electronic conductivity. In contrast, the ULL Ir anodes (Figure 2 a) do not show the same localized patters, though some locally catalyst-rich ink droplet deposition remnants are visible. Still, this represents a significant advance in PEMWE anode homogeneity.

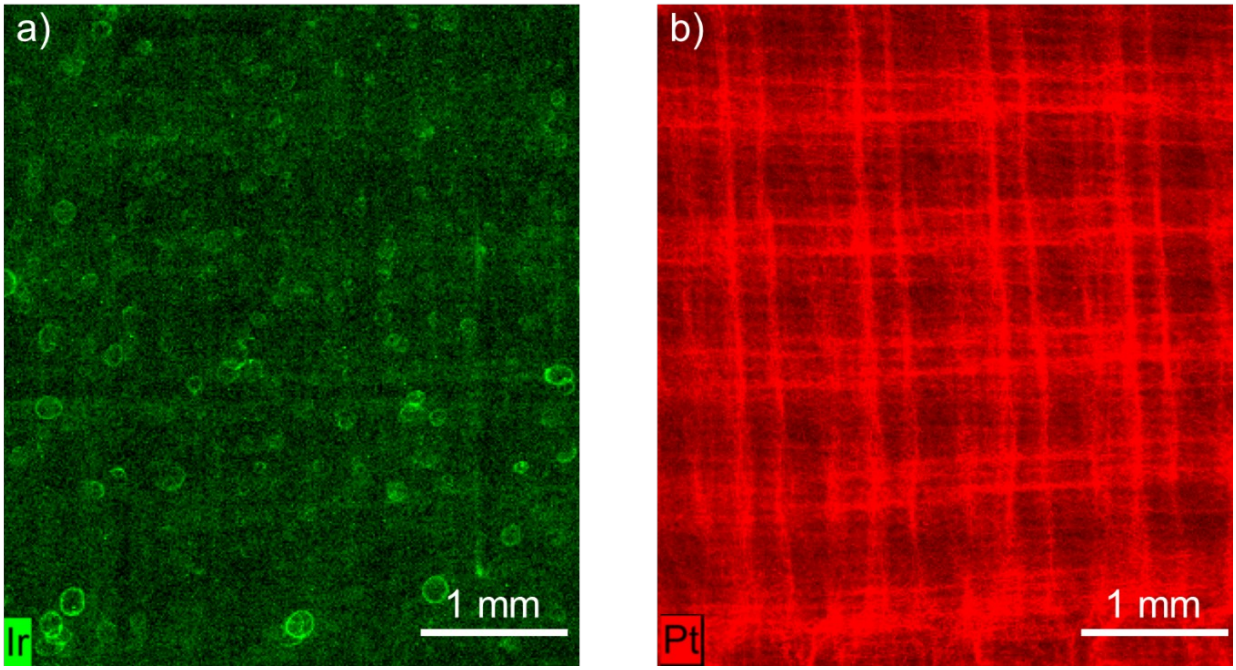

Figure 2. XRF map of a) an ULL (0.006 mg_{Ir} cm^{-2}) PEMWE anode fabricated using very dilute ink (0.08% solids), and b) PEMWE cathode (0.2 ± 0.02 mg_{Pt} cm^{-2}) using a higher concentration ink (0.27% solids).

With the ink stability, composition, and fabrication approach determined, we then focused on tuning the mesoporosity of the catalyst layer. Surface views of low and ultra-low loaded anodes, 0.05 (Figure 3 a-c) and 0.005 mg_{Ir} cm^{-2} (Figure 3 d-f), respectively, are shown. Though some cracks are observed in the lowest loaded CLs (dark spaces in Figure 3 f), they appear to cover less than 10% of the geometric area. This is a substantial improvement from unoptimized spray coatings and Mayer-rod coated[27] techniques found in the literature at equal loadings. The higher loadings (Figure 3 a-c) show excellent mesopore development and CL surface texture that should integrate well into the PTL pores, allowing for increased CL-PTL interfacial area, explored later using XCT.

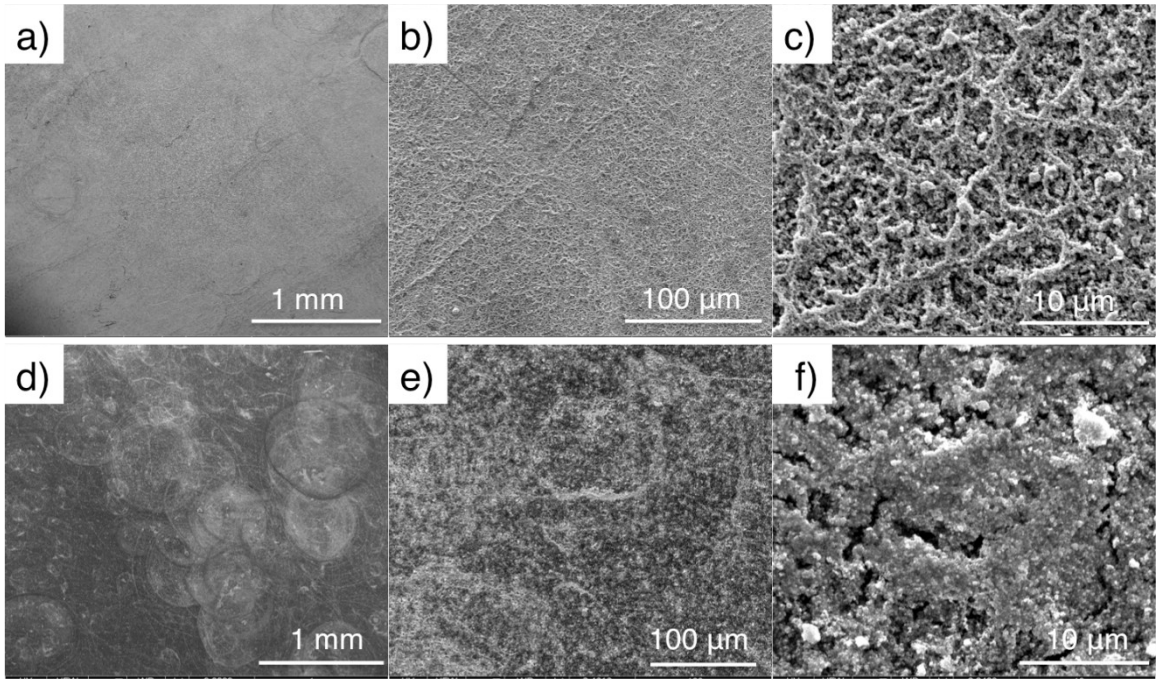

Figure 3. SEM images of anodes at different magnification a) – c): 0.05 mg_{Ir} cm^{-2}; d) – f): 0.005 mg_{Ir} cm^{-2}.

After we obtained satisfactory CL meso-morphology, we used XCT to provide information about catalyst layer thickness, distribution (ex situ XCT), and interfacial contact area and distribution between the CL and PTL under operating conditions (in operando XCT). Figure 4 shows the XCT images for the low (Figure 4 a,d) and ULL (Figure 4 b,c,e) PEMWE anodes (raw cross sectional MEA and in-plane CL XCT images and CL thickness maps and discussion are presented in Figures S6-S11). The XCT provides unparalleled in operando access to the CL-PTL interface which is essential because the interfacial contact area is dependent on localized hydration-driven swelling of the Nafion in the CL and membrane, as well as localized compression profiles due to PTL and CL irregularities. These parameters are difficult or impossible to reproduce ex-situ but are responsible for the structure of what is likely the rate-limiting interface in the cell. Shown in Figure S4, we measure a dramatic reduction in the percentage of this interface that contains PTL-CL-membrane triple phase contact from 60% at a commercial loading of 2 mg cm^{-2}, to 20% and 9% for loadings of 0.05 and 0.005 mg cm^{-2}, respectively. Visually, this trend is apparent when comparing the interfacial catalyst loadings in Figure 4 and Figure S5. Though reduction in triple phase interfacial area of 60-85% from

commercial levels seems substantial we show in Figure 1 that at the intermediate low loadings, surprisingly, there remains enough interfacial contact for satisfactory performance. Below we further breakdown the voltage losses across the loading regimes and identify the main cause of unsatisfactory performance at ULL.

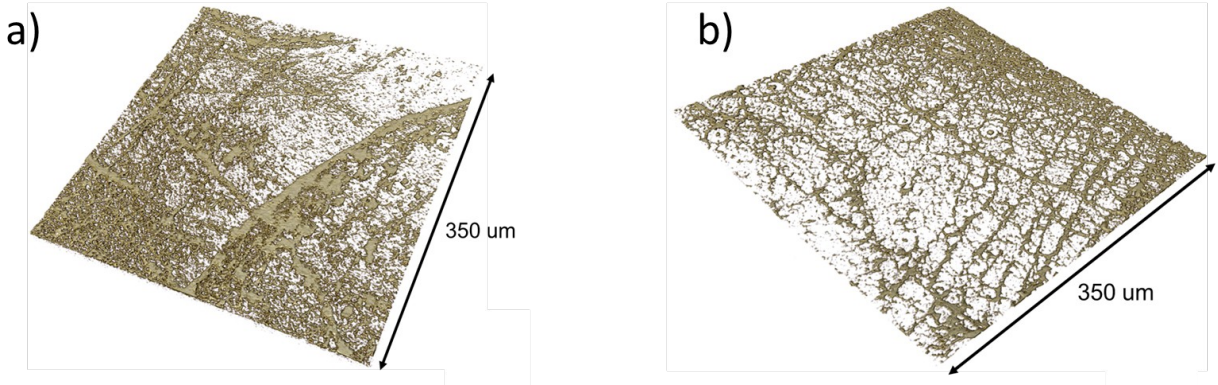

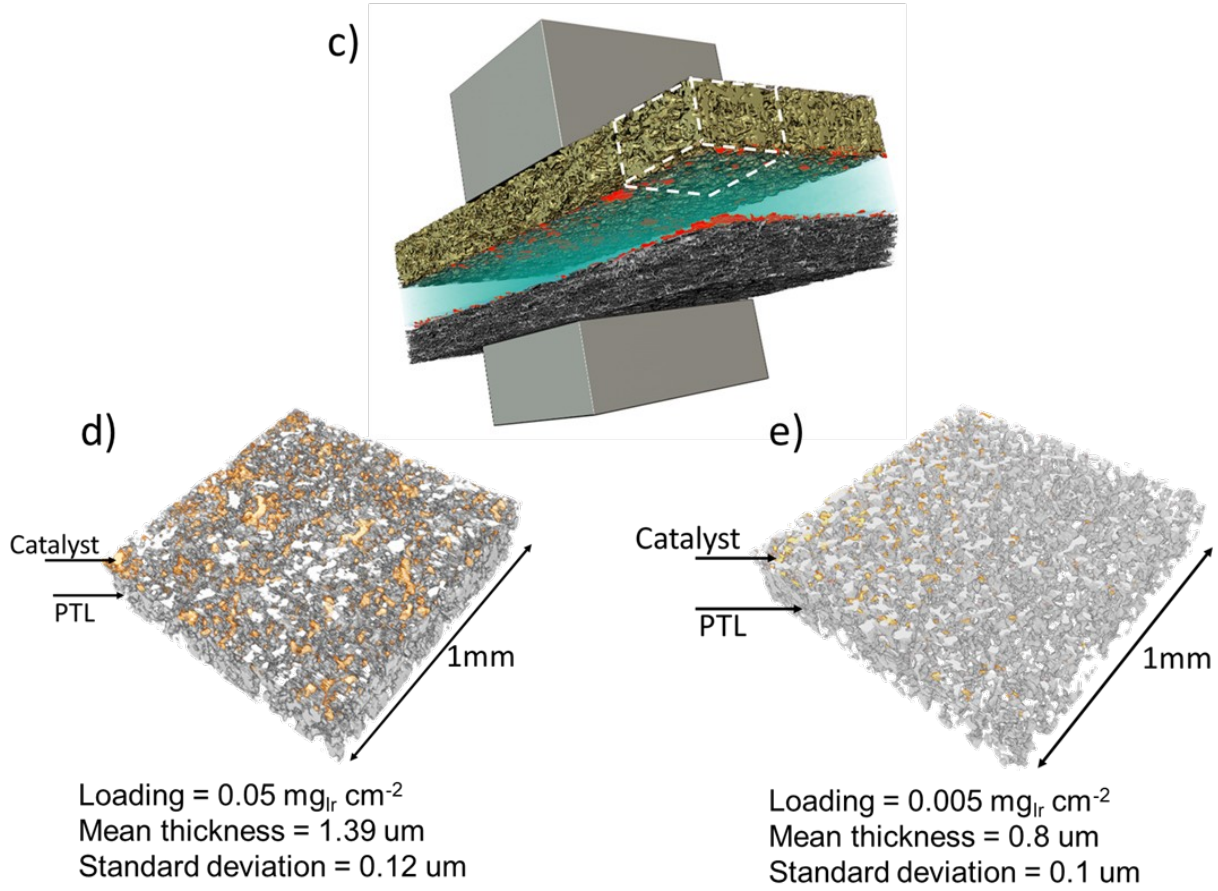

Figure 4. micro- and XCT images of 0.05 mg$_{Ir}$ cm^{-2} (a, d) and 0.005 mg$_{Ir}$ cm^{-2} (b, c, e) PEMWEs anodes. a) and b) are ex-situ micro-XCT (0.323 μm voxel^{-1}) which show CL morphology and distribution, and d) and e) are XCT (1.73 μm voxel^{-1}) taken in-operando to show the interfacial area under hydrated operating conditions. c) shows an XCT three-dimensional reconstruction of the MEA, with a white dashed box highlighting the anode locations of images d) and e), with Ir metal in the anode and Pt metal in the cathode highlighted in red.

Overpotential breakdown analysis

We conducted a parametric study of anodic Ir loading within mesostructured PEMWE CL's to identify performance trends extending into the low and ULL regime and determine the minimum viable Ir content for PEMWE membrane electrode assemblies (MEAs). The anode Ir loading was varied from 0.17 to 0.0035 mg$_{Ir}$ cm^{-2} while holding all other MEA materials and cell testing conditions constant, while current-voltage polarization curves were collected to measure performance. The uncorrected polarization curves are presented in Figure 1, while the iR-corrected polarization curves and extracted kinetic, ohmic, and mass transport overpotentials are

presented in Figure S12.

Ohmic losses

We first discuss ohmic losses as they were largely unimpacted by Ir loading. The ohmic overpotential (Figure S12 c) remained consistent, with HFR ranging between 125 – 143 mΩ cm^2, across all MEAs with no discernable trend with Ir loading or CL thickness. Large changes in ohmic overpotential were not expected even if the contact between PTL and CL changed at ULL since the majority of the ohmic overpotential is a result of the thick Nafion™ 117 membrane and cell contact resistances. In the literature, some increase in HFR has been reported at lower catalyst loadings[27]. This increase has been attributed to less homogeneous and/or thinner CLs that are not in direct contact with the PTL. Combined with low in-plane electrical conductivity in the CL this results in an increase in CL electronic resistance and an increase in HFR. Here these effects are largely hidden by the large resistance of thick N117 membrane, as well as slight variance in cell assembly.

Kinetic losses at low Ir loading

The kinetic, or activation, overpotentials were extracted from the iR-corrected polarization curves using a Tafel analysis (inset Figure 1), and are presented in Figure S12 b. The Tafel slope and exchange current density were calculated assuming the kinetically-dominated region was below 40 mA cm^{-2} for the 0.0035 mg_{Ir} cm^{-2} loading, and below ~80 mA cm^{-2} for all other loadings because the polarization curves in these ranges were sufficiently linear while also providing enough datapoints for a quality regression analysis. As shown in the inset of Figure 1, the calculated Tafel slopes at the 0.17 and 0.039 mg_{Ir} cm^{-2} loadings were generally lower than other literature values, which have a minimum of ~45 mV dec^{-1} [27,36,37]. A Tafel slope of < 40 mV dec^{-1} is especially notable when evaluating against studies using comparably low loadings where Tafel slopes of over 70 mV dec^{-1} have been recorded[38]. The improvement in Tafel slope seen in this work is attributed to the uniformity of the CL (cf. Figure 3) produced as a result of the mesostructuring and better interfacial contact with the PTL than a non-uniform CL. As a previous study indicated, better contact between the CL and PTL leads to higher catalyst utilization[35]. While much work is focused on tailoring the PTL side of the PTL-CL interface

through microporous layers[35], PTL pore size[39,40] to land ratios[41–43], and operating conditions[44], this result shows that effort paid towards the CL side of the interface can improve kinetic performance independent of these PTL modifications, and even result in previously unattained kinetic activity. Thus, it is critical that attention be concurrently paid towards optimizing the CL side of this critical interface.

As the Ir loading was reduced the Tafel slope increased monotonically from 38 mV dec^{-1} at 0.17 mg_{Ir} cm^{-2} to 70 mV dec^{-1} at 0.0035 mg_{Ir} cm^{-2}. This increase in Tafel slope resulted in an increase in overpotential at kinetically controlled current densities, e.g. at the lowest measured current density of ~4 mA cm^{-2} the overpotential increased from 235 to 284 mV from the 0.17 mg_{Ir} cm^{-2} to the 0.0035 mg_{Ir} cm^{-2} loadings, respectively. This 49 mV difference represents a 20% increase in overpotential at the lowest measured current density and indicates a substantial decrease in kinetic performance at ULL. It has been hypothesized that this increase in overpotential at ULL is due to a non-homogeneous CL in which significant portions of the catalyst are not in electronic contact with the PTL[27,33]. These catalyst "islands" in a low-loaded CL reduce the available active sites. Meaning, for a low-loaded CL to operate at the same current as a high-loaded CL its active sites must operate at a higher reaction rate, as opposed to recruiting more active sites as a higher loaded CL would[45]. The difference being that increasing kinetics result in an exponential decrease in overpotential, whereas recruiting more active sites requires a linear ohmic overpotential to drive electrons further into the CL. The 20% increase in kinetic overpotential, then, indicates that the lower loaded CLs are utilizing their available sites more than higher loaded CLs, and are demanding an increase in site specific reaction rate. This higher utilization of the CL will become more evident in forthcoming sections.

It is clear the kinetically dominated current density range is dependent on the catalyst loading and must be adjusted for MEAs with ULL. The common assumption of kinetically limited behavior below current densities of ~100 mA cm^{-2} does not hold for these low loadings, and a geometric area normalized current is unlikely to well represent the losses in this loading range due to localized effects.

Mass Transport losses

The highest loaded MEA (0.17 mg_{Ir} cm^{-2}) had the lowest mass-transport overpotential at all current densities, and in general as Ir loading was reduced the mass-transport overpotential increased, Figure S12 d. The major difference between the MEAs is the onset of a severe mass transport limitation at ULL, at approximately 1.4 A cm^{-2} for the 0.011 mg_{Ir} cm^{-2} loaded MEA, see Figure 1 and Figure S12 a and d. As the Ir loading is further reduced, the mass-transport limitation occurs at increasingly lower current densities, approximately 200 and 100 mA cm^{-2} for the 0.006 and 0.0035 mg_{Ir} cm^{-2} loadings, respectively. Since the PTL, membrane, and cell hardware were all unchanged, the earlier onset must derive from local changes in the CL and/or its interface with the PTL, as shown in Figure 4. Investigating this interface using in-operando XCT we see the fraction of the PTL-CL interface where catalyst is present decreases from 60% at 2 mg_{Ir} cm^{-2} commercial-level loadings, to 20% and 9% at 0.05 and 0.005 mg_{Ir} cm^{-2}, respectively (Figure S4). This decrease in triple phase contact area (TPCA) has direct implications on the distribution of the OER in the CL, and associated oxygen removal from the active sites. As the TPCA decreases the number of active sites decreases, and higher local reaction rates are necessary to maintain total cell current relative to higher loaded MEAs. These higher local oxygen production rates thus become an issue for ULL MEAs when the oxygen production rate outpaces oxygen transport away from the sites, and oxygen bubbles begin to accumulate causing severe mass transport limitations. One way this occurs in thin CLs at ULL is through a reduction in cross-sectional in-plane CL area available for water and oxygen transport from PTL pore to the CL below the PTL land. This reduction in transport area is believed to lead to severe mass-transport limitations due to excessive oxygen bubble coverage in the anode[31].

To quantify the impact of accumulation of oxygen in the electrode on cell performance we analyzed the XCT images in several regions of the anode channel. At current densities above approximately 3 A cm^{-2} the ULL electrode showed lower oxygen content in the channel than at higher loadings, Figure 5, indicating that oxygen was accumulating in either the PTL or CL. Accumulation in either region is problematic as oxygen in the PTL impedes water transport to the CL, while oxygen in the CL deactivates catalyst sites. Imaging techniques with higher resolution are necessary to identify where exactly the oxygen is accumulating, but it is clear from these measurements that oxygen removal is impeded for ULL electrodes and must be addressed to avoid severe mass transport limitations. Furthermore, to demonstrate the phenomena we conducted a variable relaxation time study. Within the OER region (1.2-2 V vs. RHE) we sweep the voltage at 50 mV s^{-1}, while in the non-OER region (0.05-1.2 V vs RHE) we alternated between 20 and 50 mV s^{-1}. This resulted in a relaxation time of 115 and 46 s for the 20 and 50 mV s^{-1} sweep rates, respectively. Figure S13 shows that allowing the anode more time to clear the generated oxygen immediately results in performance improvement as oxygen leaves the CL, and then performance declines as oxygen evolves and accumulates in the CL upon subsequent cycles.

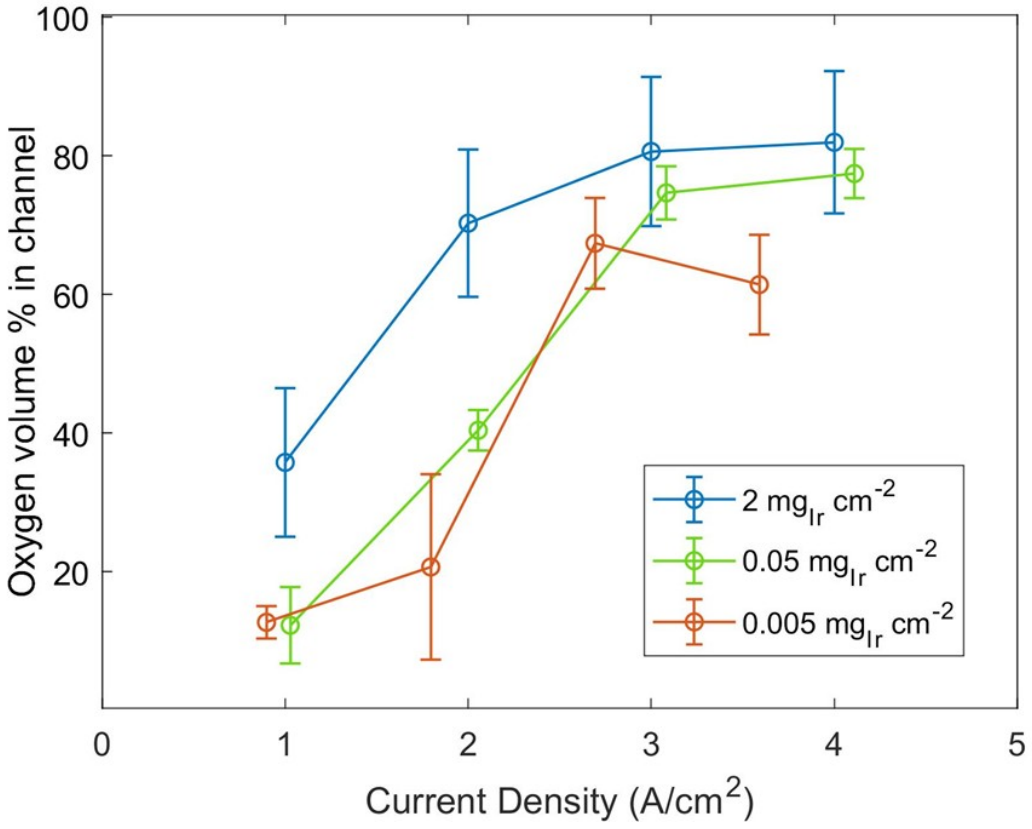

Figure 5. Impact of anode Ir loading and current density on channel oxygen volume fraction. At a current density of ~3.5 A cm^2 the ULL MEA (0.005 mg$_{Ir}$ cm^{-2}) had less oxygen present in the channel than higher loaded MEAs, indicating that oxygen was accumulating in either the PTL or the CL

Specific current analysis

To better account for the loading dependent nature of the losses previously described, we now normalize the cell current by the mass of anodic Ir in the MEA. The Ir catalyst used in this work (TKK ELC-0110 SA=100, XRD, XPS, TEM, and RDE characterization presented in Figure S15) is a high surface area (100 m^2 g^{-1}) bulk oxide with Ir^{+4} surface oxidation state (IrO_2). We normalize cell current only by the Ir element, not the total mass of catalyst which would include incidental oxygen or other elements. The results are potential vs specific current (A mg$_{Ir}^{-1}$) plots that more closely elucidate the performance difference between active sites as opposed to active geometric area. Figure 6 shows the same polarization curves as in Figure 1, except that the current has been normalized by Ir mass (A mg$_{Ir}^{-1}$) instead of geometric area (A cm^{-2}). We note

that we omit electrochemically active surface area (ECSA) normalization due to the controversies around obtaining accurate and representative values for non-Pt based materials[46].

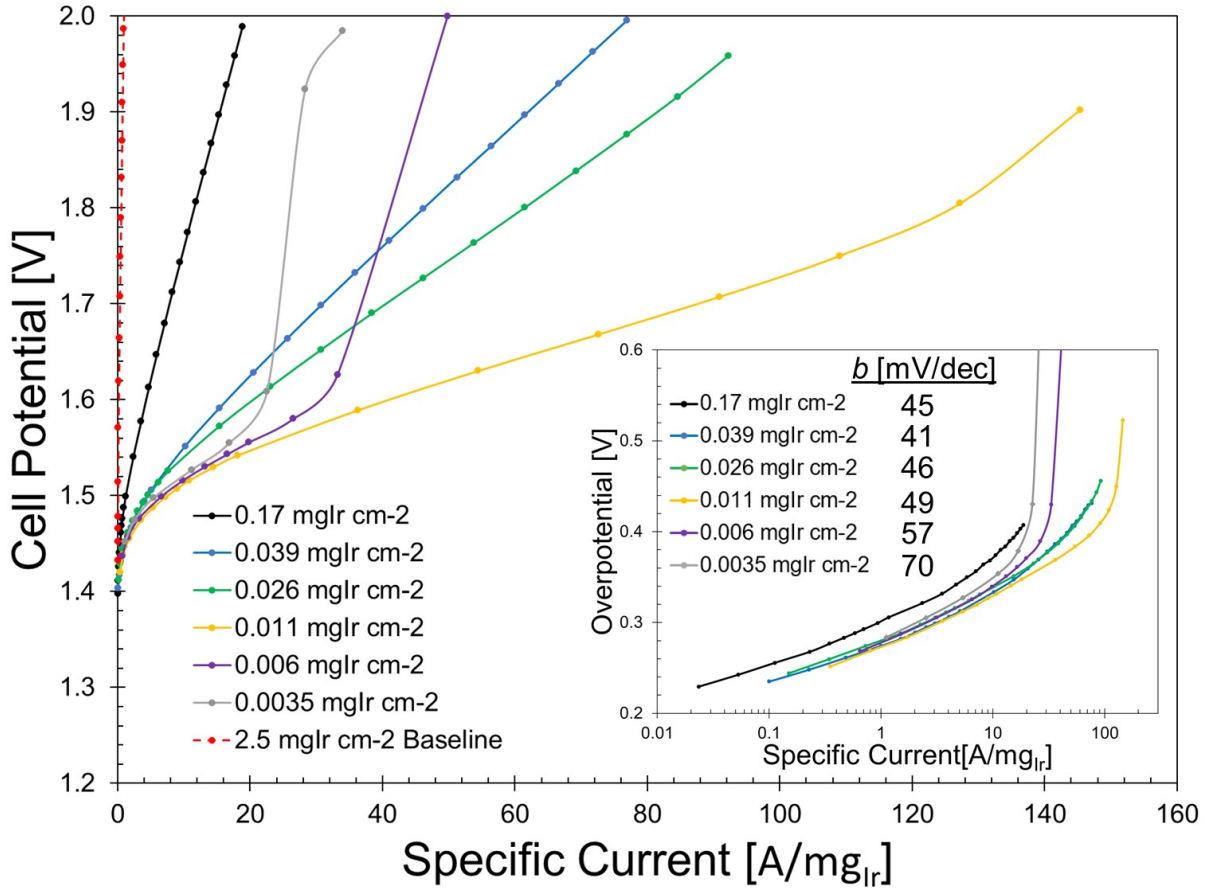

Figure 6. PEMWE polarization curves using specific current at different Ir loadings under constant ionomer/catalyst ratio of 0.116. Loadings are reported as iridium metal cm^{-2}, measured using XRF. Inset shows Tafel plot using Ir-specific current [A mg$_{Ir}^{-1}$] as the reaction rate coordinate. Cathode Pt loadings were kept at 0.2 ± 0.02 mg cm^{-2} for all tests. Nafion™ 117 was used as the membrane. The red dashed line represents baseline performance of a commercial 2.5 mg$_{Ir}$ cm^{-2} loaded MEA (Greenerity E400) round-robin tested at 5 independent laboratories for the IEA Electrolysis Annex 30[32].

The change in current normalization reveals a different picture of the catalyst utilization as the highest loaded MEA showed the lowest catalyst utilization at all Ir-specific currents, though still performed exceptionally well vs. the commercial cell. The catalyst utilization improved as Ir loading was reduced until 0.011 mg$_{Ir}$ cm^{-2}, at which point the onset of the mass-transport limitation was seen at a very high specific current of over 130 A mg$_{Ir}^{-1}$. Then, upon further reduction of Ir loading, onset of the severe mass transport limitation occurred at

increasingly lower Ir-specific current. Thus, a loading of 0.011 mg_{Ir} cm^{-2} is optimal for catalyst utilization in this study. At a HHV-based efficiency of 89% (1.6 V vs. RHE), the highest loaded MEA (0.17 mg_{Ir} cm^{-2}) operated at an Ir-specific current of ~ 4 A mg_{Ir}^{-1} while the 0.011 mg_{Ir} cm^{-2} MEA achieved ~40 A mg_{Ir}^{-1}, representing a 16- and 166-fold improvement in catalyst mass activity over the commercial cell which operated at ~0.24 A mg_{Ir}^{-2}. The improvement is further amplified at higher potentials, e.g. at 1.8 V the optimal loaded MEA recorded an Ir mass activity over 250 times higher than the commercial cell. To investigate why there is such an extreme difference in utilization vs Ir loading, and gain insight into the origin of the optimal loading level, we present a specific current based overpotential breakdown in the following sections and in Figure S14.

Kinetic

Basing the Tafel analysis on Ir-specific current (inset Figure 6) instead of current density (inset Figure 1) hints at a loading threshold for optimal electrode utilization. In the studied IrO_2–PTL system there seems to be a loading at which point the catalyst in the anode is near fully utilized and the kinetics follow a common Tafel profile, qualitatively collapsing into a single curve. In this study this occurs at a loading of 0.039 mg_{Ir} cm^{-2}, after which reductions in loading do not incur further kinetic advantage. The highest loaded MEA (0.17 mg_{Ir} cm^{-2}) operated with an Ir-specific current-based Tafel slope of 45 mV dec^{-1} and an associated Ir-specific exchange current of 0.2 μA mg_{Ir}^{-1}. The next lowest loaded MEA (0.039 mg_{Ir} cm^{-2}) also had an Ir-specific exchange current of 0.2 μA mg_{Ir}^{-1}, indicating that the inherent activity of the IrO_2 catalyst was unchanged between the two electrodes. However, the 0.039 mg_{Ir} cm^{-2} loaded MEA showed higher mass normalized kinetic activity, measured as having a lower Tafel slope of 41 mV dec^{-1}. This is an impressive result since the total Ir content was reduced by 77%, yet the kinetic performance improved on a mass basis. Stated another way, a higher loaded MEA cannot fully utilize the catalyst within the electrode and incurs a mass-normalized overpotential penalty for having excess underutilized catalyst.

Mass-transport

The limitation to endlessly reducing the Ir loading seems to be the onset of a severe mass-transport limitation that is localized near the reaction sites themselves, likely the oxygen

obfuscation issue previously identified. The first time the limitation is seen is at an extremely high Ir-specific current density of over 130 A mg_{Ir}^{-1} in the 0.011 mg_{Ir} cm^{-2} loaded MEA. This is the highest specific current measured in the study and is a reasonable location for a mass-transport limitation to arise, especially given the evidence that local oxygen bubble formation plays a role in this transport limitation. Though we are restricted to triple phase contact area and channel oxygen concentration measurements at 0.05 and 0.005 mg_{Ir} cm^{-2}, we can use these as bounding cases to examine the electrochemical MEA performance in the ULL regime. As previously mentioned, channel oxygen concentration decreases from 0.05 to 0.005 mg_{Ir} cm^{-2}, indicating oxygen buildup in either the PTL or CL, while at the same time the triple phase contact area decreases from 20% to 9% for the 0.05 to 0.005 mg_{Ir} cm^{-2} MEAs as well. Thus, the lower number of active sites present are required to operate at higher local reaction rates, increasing the local oxygen production rate to the point that oxygen removal from the PTL-CL system struggles to keep up. The higher fidelity electrochemical MEA measurements show these converging factors are optimized near a loading of 0.011 mg_{Ir} cm^{-2}. There is likely a parameter that relates oxygen bubble removal and reaction distribution that governs the lower extent where ULL is feasible. Identifying this parameter and its functional dependencies will provide key insights into how to reduce mass transport limitations in the ULL regime.

Overpotential distribution

To better visualize the difference between the area (current density) and mass (specific current) current normalization techniques, the overpotential distribution vs. current density (Figure 7 a-c) and specific current (Figure 7 d-f) is presented. The area normalized distribution shows a rise in mass-transport overpotential share at lower current densities as loading is decreased, e.g. 1500 mA cm^{-2} in Figure 7 b. As the whitespace in Figure 7 c conveys, the maximum current density achieved by the 0.0035 mg_{Ir} cm^{-2} is likely insufficient for practical applications. However, the optimal loading of 0.011 mg_{Ir} cm^{-2} from a specific current perspective is clearly evident in Figure 7 e. At this loading, the majority of the overpotential is used for kinetics well past 100 A mg_{Ir}^{-1}, whereas only ~40% of the overpotential goes towards kinetics for the highest loaded MEA at comparably paltry 20 A mg_{Ir}^{-1}. Though at 2 V the 0.011 mg_{Ir} cm^{-2}

loaded MEA's aera normalized hydrogen production rate is approximately half that of the 0.17 mg_{Ir} cm^{-2} loaded MEA (Figure 7 a vs. b), it produces over 6 times more hydrogen per mg_{Ir} (Figure 7 d vs. e).

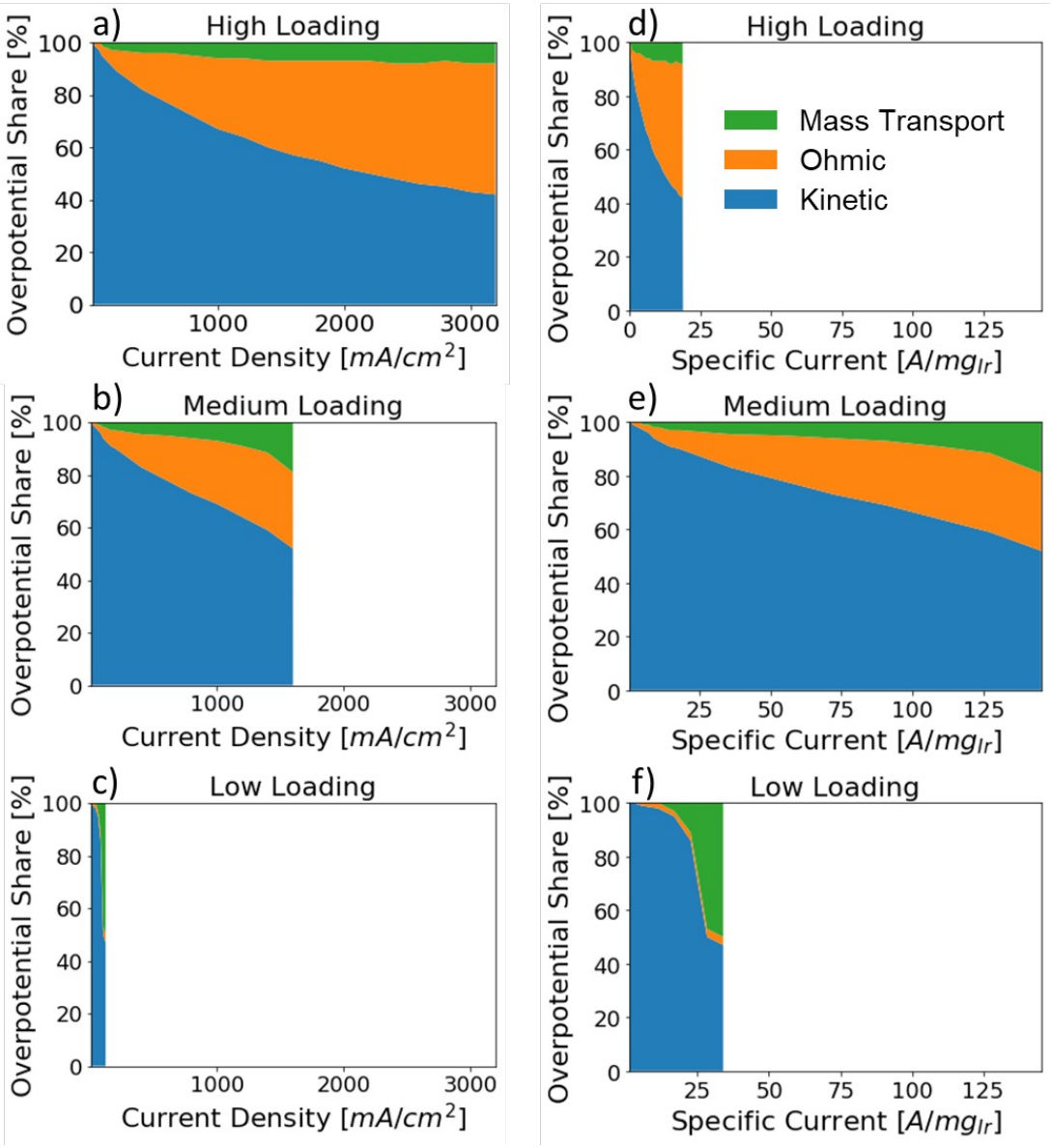

Figure 7. Distribution of kinetic, ohmic, and mass transport overpotential vs current density for loadings of a) 0.17 mg_{Ir} cm^{-2}, b) 0.011 mg_{Ir} cm^{-2}, and c) 0.0035 mg_{Ir} cm^{-2}, compared to the same distribution vs specific current for loadings of e) 0.17 mg_{Ir} cm^{-2}, f) 0.011 mg_{Ir} cm^{-2}, and g) 0.0035 mg_{Ir} cm^{-2}. Area normalized current density (a-c) shows the mass transport overpotential increasing at lower current densities as the loading is decreased, indicating earlier onset of transport limited conditions. However, the mass normalized specific current plots (e-f) reveal the optimal loading of 0.011 mg_{Ir} cm^{-2} (e) primarily uses the overpotential to drive kinetics at catalyst utilizations well beyond what is achievable at higher and lower loadings.

Pathway to Complete Energy Sector Decarbonization

To further investigate the impact that ULL PEMWEs can have on deep decarbonization, we revisit the Ir-specific power. As seen in Equation 1, Ir-specific power can either be improved by increasing the operational current density (at 1.6 V, as defined) or decreasing the iridium catalyst loading. Examples of both approaches can be found in the literature (cf. Figure 8). Increasing the current density, however, requires increasing the cell potential beyond currently acceptable levels (around 2 V), which leads to lower hydrogen production efficiencies, increased degradation rates, and higher power supply costs (which account for a significant portion of the system cost)[47]. Therefore, loading reductions seem favorable.

Commercial electrolyzers have an Ir-specific power, as defined above in Equation 1 of ~2 MW kg_{Ir}^{-1} [22]. If half of the global Ir supply, 3.6 t y^{-1}, was used for PEM electrolysis the feasible yearly electrolyzer deployment would be 7.2 GW per year. Since near-term electrolysis deployment favors decarbonizing the natural gas sector[15] we will investigate if this level of deployment is sufficient to decarbonize the sector by 2050. The global energy consumption of natural gas in 2016 was 60 EJ (~ 57 quads), and has been increasing linearly at a rate of 750 PJ a^{-1} [48]. Extrapolating this consumption to 2050, the expected global gas consumption is 85 EJ a^{-1}, or a yearly averaged power consumption of 2.7 TW. Given the available Ir supply of 3.6 t a^{-1}, a cumulative total of 108 t of Ir will be available for PEMWEs by 2050 (30 years of deployment). Achieving the necessary global hydrogen production rate would require an Ir-specific power of approximately 25 MW kg_{Ir}^{-1}, an intensification of 13-fold from today. Both Babic et. al.[22] and Bernt et. al.[27] have recently completed similar analysis. Babic et. al. investigated using PEM electrolysis as the dominant global renewable energy storage medium at an unspecified future date, while Bernt et. al. focused on decarbonizing the global transportation sector by 2100 (adjusted here for a 2050 decarbonization target). They arrived at similar targets of 36 and 42 MW kg_{Ir}^{-1}, respectively, when correcting for different Ir supply assumptions. These analyses show that satisfying the combined natural gas, transportation, and electricity storage sectors would require an Ir-specific power of ~100 MW kg_{Ir}^{-1}. Figure 8 investigates where the research community is relative to these targets using the Ir loading and current density to define the

parameter space, in line with Equation 1. The area shaded in green highlights where the 25 MW kg_{Ir}^{-1} (natural gas sector) target is met. The performance of low and ultra-low loaded PEMWE studies identified in the literature is overlaid in the colored markers.

a)

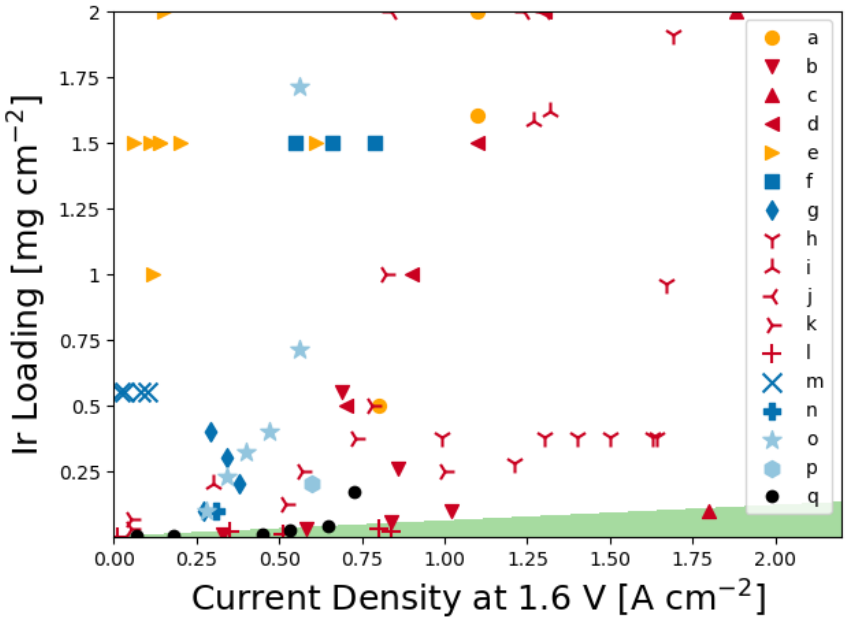

b)

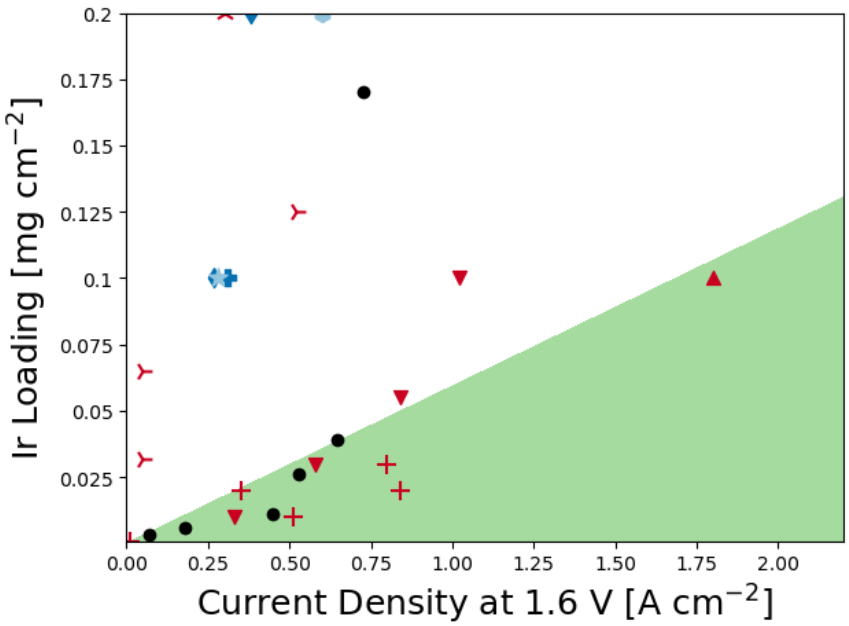

Figure 8. a) Operational map showing the combinations of current density and catalyst loading necessary to achieve an Ir-specific power of 26 MW kg_{Ir}^{-1}, and where this work (black circles) measures in relation. The area shaded in green achieves this target, while the white area does

not. b) shows a magnification of the ULL region where the target Ir-specific power is achievable. The symbol color refers to membrane thickness: dark blue ~180 um, light blue ~130 um, orange ~90 um, red ~ 50 um. References for the data are as follows: a-[49], b-[50], c-[51], d-[52], e-[53], f-[54], g-[25], h-[55], i-[27], j-[56], k-[26], l-[57], m-[58], n-[17], o-[24], p-[59], q-this work.

Extrapolating from the findings of Figure 8 reveals that an electrolyzer with an anode Ir loading of 1 mg cm^{-2} (roughly half of commercial loadings) must operate at over 17 A cm^{-2} to reach the annual deployment goals. This level of catalyst utilization is not feasible at reasonable potentials with current catalysts and MEA fabrication techniques. Instead, Ir loadings below approximately 0.1-0.2 mg_{Ir} cm^{-2}, an order of magnitude lower that current commercial loadings, are necessary to realize the deployment targets at today's achievable current densities (2 A cm^{-2}). Other approaches such as the nanostructured thin film catalyst developed by 3M company[26], reactive spray deposition technology by the University of Connecticut[17], or the reverse-opal structure produced by Park et al[57], though showing very promising results, are the exception as they rely on novel manufacturing processes that may be too slow or expensive to meet demand.

As shown, all the cells in this work (black circles), except for the 0.17 mg_{Ir} cm^{-2} loaded cell, meet the 25 MW kg_{Ir}^{-1} performance target. This is especially notable since we used commercially relevant Nafion™ 117 membranes whose ~180 um thickness allows for differential pressure operation while limiting hydrogen crossover, essential for commercial operation. The literature studies that achieve the 25 MW kg_{Ir}^{-1} target all use 50 μm membranes that decrease crossover resistance and mechanical robustness to differential pressure. These studies also relied on electrode fabrication processes that took over 30 hours for a 5 cm^2 electrode[57], or carbon based anode components that have limited OER durability[50,51]. The electrode fabrication in this work took 30 minutes or less and used only commercially supplied OER stable components and is readily incorporated with thinner membranes to further improve efficiency, when and if electrolyzer stack manufacturers were to integrate these in commercial systems.

We defined the specific current targets at a HHV-based conversion efficiency of 89% to eliminate as much wasted electrical feedstock as possible. However, this constraint does not take into consideration electrode stability which would result in more stack replacements, other capital vs. hydrogen production rate optimizations, and limits potential impact that could be

realized at lower conversion efficiencies. To address this constraint, we present the measured specific power for all cell potentials (conversion efficiencies) in Figure 9.

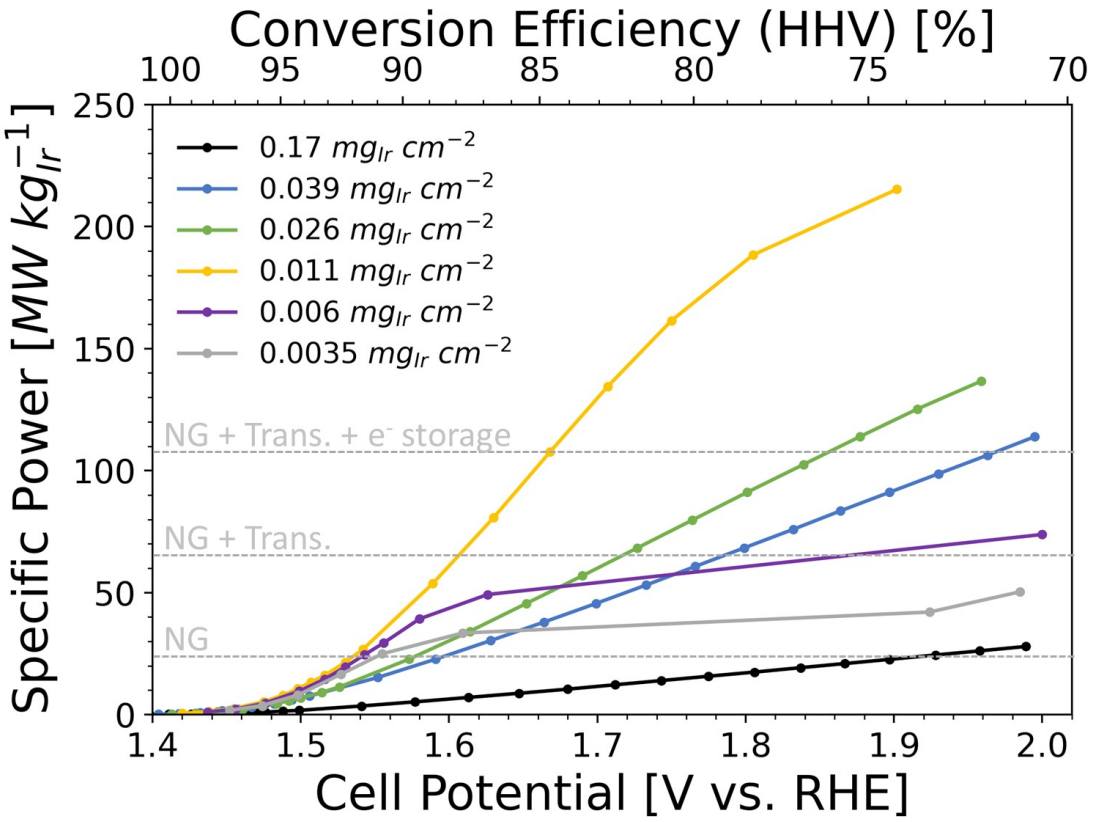

Figure 9. This plot shows the specific power of the anode Ir loadings studied vs. uncorrected cell potential and associated higher heating value-based energy conversion efficiency. The grey dashed lines mark the specific power targets necessary to decarbonize the natural gas (NG) sector, NG and transportation sector combined, and the NG, transportation, and electricity storage sectors combined as calculated in this work, and by Babic et al.[22] and Bernt et al.[27].

As seen, PEMWEs with anodes containing the optimal loading of 0.011 mg_{Ir} cm^{-2} could meet the combined natural gas and transportation sector energy demand by 2050 at a HHV-based efficiency of ~88% using only half of the annual Ir supply. The same cells could satisfy the natural gas, transportation, and energy storage sectors by 2050 at an efficiency of ~85% (1.67 V vs. RHE). At lower conversion efficiencies all sectors could also be satisfied by 0.026 mg_{Ir} cm^{-2} and 0.039 mg_{Ir} cm^{-2} loaded cells, which will likely have better durability.

Conclusion

In this work, we demonstrate a pathway to enabling decarbonization of the natural gas, transportation, and energy storage sectors by the year 2050. By reducing the Ir loading to below 0.04 mg cm^{-2}, two orders of magnitude lower than commercial PEMWEs, only half of the global Ir supply would be consumed. To achieve this target, the mesostructure of anode electrodes demonstrated in this manuscript were first optimized, allowing them to exceed published cell-level performance of low and ULL PEMWEs.

The anode Ir loading in PEMWEs was systematically reduced to ULL in the range of 0.17 to 0.0035 mg cm^{-2}, while using commercially available cell components, catalysts, and fabrication methods. Effort was paid towards optimizing the fabrication process of the anode CL so that a well distributed, continuous, CL was produced, even at ultra-low catalyst loadings. The current density applied voltage breakdown revealed impressive electrode kinetics at low Ir loading, with a 0.039 mg_{Ir} cm^{-2} loaded electrode measuring a Tafel slope of 39 mV dec^{-1}. Electrode kinetics were, however, dependent on loading, and were greatly degraded at ULL; e.g. a 0.0035 mg_{Ir} cm^{-2} loaded electrode was measured to have a Tafel slope of 70 mV dec^{-1}. Ohmic losses were independent of catalyst loading, and measured HFR did not show a trend consistent with loading. A severe mass transport limitation was seen and occurred at lower current densities for lower loaded electrodes. In operando micro-X-ray computed tomographic measurements hints that oxygen bubble obstruction of the anode Ir catalyst sites was the likely cause. Mass-based specific current overpotential breakdown analysis revealed that mass-normalized electrode kinetics were qualitatively similar for anode electrodes with loadings lower than 0.039 mg_{Ir} cm^{-2}. Higher loadings resulted in a higher mass-based kinetic overpotential, indicating a penalty required for including extra underutilized catalyst. For ULL MEAs, high specific currents are realized at low cell currents, meaning that most of the cell overpotential is going towards kinetics, and not ohmic losses. Though the onset of the mass-transport limitation was better correlated to mass normalized current than area normalized current, the trend was still not fully captured by the specific current analysis. This indicates the mass transport limitation is localized closer to the reaction sites themselves and requires further analysis and research. We postulate that durability issues at low loadings are a result of this localized mass transport limitation. These limitations must be understood and mitigated if we are limited to making the best use of Ir resources to enable the complete offset of fossil-based natural gas by electrolytically produced

hydrogen by the year 2050.

Experimental Materials and Methods

Catalyst Coated Membrane (CCM) Fabrication

Particle size and ink stability were evaluated using a Zetasizer (Malvern Instruments). Anode ink was prepared by mixing commercially available iridium oxide (TKK ELC-0110 SA=100) with water, ethanol, and n-propanol at a ratio of 1:1:2 by volume, and Nafion™ ionomer solution (5 wt%, Ion Power D521). Initial characterization of the TKK catalyst including TEM imaging, XRD, XPS, and RDE analyses are included in Figure S15. Ionomer to iridium ratio and mass of iridium were varied depending on the study. The anode ink was immersed in an ice bath, sealed with parafilm, and sonicated using a horn sonicator (CEX500, Cole-Parmer) at 30% of power for 30 min prior to deposition. The cathode ink was prepared by mixing platinum supported by carbon catalyst (TKK TEC10V50E) with equal parts water and n-propanol, and Nafion™ ionomer solution (5 wt%, Ion Power D521). The cathode inks were then sonicated at constant temperature of 10 °C in a bath sonicator for 30 minutes prior to deposition. The bath sonicator was retrofitted to include a water temperature controller and we found that 10 °C was sufficient to keep the Pt from oxidizing the solvents in the ink and avoiding agglomeration and settling. The horn sonicator's sample compartment was not large enough to include such a retrofit, so we instead used a simple ice bath resulting in slightly different sonication temperatures. The volume of both inks was kept constant during the entire study to minimize the impact of ink preparation on cell performance. The inks were prepared immediately prior to being spray-deposited onto Nafion™ N117 membranes using a Sono-Tek ultrasonic spray coater and a 5 cm^2 rienforced Teflon stencil to ensure catalyst was only present on the 5 cm^2 active area. The Nafion™ perfluorosulfonic acid membranes (N117, Ion Power) were prepared by soaking in DI water at 90 °C for one hour and followed by immersion in 0.5 M HNO_3 (ACS Reagent, Sigma-Aldrich) for one hour at room temperature to remove impurities and protonate the sulfonic-acid groups. Finally, the treated membranes were rinsed three times using DI water to remove excess acid and stored in DI water until catalyst coating is performed. The Sono-Tek sonication was set to 120

kHz, and the spray deck was modified with a porous aluminum plate and vacuum pump that pulled the membrane flat. The spray deck was held constant at 90 °C. The cathode and anode deposition process were similar, with spray passes held constant where possible. After spray coating, the precious metal loading was measured using X-ray fluorescence (XRF) (Bruker M4 Tornado). The XRF was calibrated using commercial standards (Micromatter Technologies Inc.) and calibration curves are shown in the supporting information.

Cell Assembly. CCMs with 5 cm^2 active area were assembled in single cell hardware (Fuel Cell Technology) with a graphite single channel serpentine flow field on cathode and platinized titanium parallel flow field on anode. The CCM was rehydrated at room temperature in DI water before it was assembled into the cell. Teflon gaskets were used on anode and cathode, respectively. Carbon paper without microporous layer (Toray 120) is used as cathode GDLs. Platinized sintered titanium (obtained from Proton OnSite/NEL) is used as anode porous-transport layers (PTLs). The appropriate thickness PTFE (McMaster-Carr) gaskets are used to obtain 20% compression in GDLs, while thickness-matched gasket is used for the Ti-PTL. A torque of 4.5 Nm is applied to the cell to ensure proper sealing.

Cell Testing. A multichannel potentiostat (VSP300, Biologic) equipped with electrochemical impedance spectroscopy (EIS) and a 20 A booster was used for all electrochemical tests. The test station used is a modified Fuel Cell Technology (FCT) test stand; the modification is an addition of a water recirculation system for the electrolyzer mode testing. Before any electrochemical testing, hot DI water was supplied at 80 °C at 125 ml min^{-1} on the anode side and the cell was allowed to preheat for 30 min, after which an auxiliary heater is used to further heat up the cell to 80 °C. Temperature infirmity across the cell was verified with an IR camera. 100 mL min^{-1} of dry H_2 (no water flush was supplied to the cathode) was supplied to the cathode at ambient pressure to ensure a pseudo-steady reference electrode for electrolyzer operation. Conditioned cyclic voltammetry (CV) was taken via scanning between 1.2 and 2 V at 50 mV s^{-1} for ten cycles before recording polarization curves and electrochemical impedance. The polarization curve was taken by holding at various constant cell currents for 130 s while recording cell voltage. The impedance was measured in a galvanostatic mode by applying an AC current perturbation between 200 kHz – 100 mHz to the cell and measuring its voltage response at each polarization

step. The amplitude of the AC current was chosen for each step to obtain a sufficient signal to noise ratio, while keeping the perturbation small enough to ensure a linear system response. The Ir cyclic voltammetry was measured by cycling electrode form 0.05 – 1.2 V at 50 mV s^{-1} at 80 °C with DI water and H_2 fed to anode and cathode, respectively.

Overpotential analysis. The cell voltage E_{cell} is composed of the sum of the reversible cell potential E_{rev}^0 and the three main overpotential η_i:

$$E_{cell} = E_{rev}^0 + \eta_{kin} + \eta_\Omega + \eta_{mt} \quad Equation\ SEQ\ Equation \text{¿}\ ARABIC\ 2$$

where η_{kin} is the kinetic, η_Ω the ohmic and η_{mt} the mass transport overpotential. Since HER is more favorable in kinetics and mass transport under current testing conditions compared to OER, the overpotential analysis only considers the OER side.

At a temperature of 80 °C, the saturation pressure of H_2O is 0.47 bar_a. For liquid water, the activity of water, $a(H_2O)$, is one, while the activity of the gaseous species is represented by the ratio of their partial pressure to the standard pressure of 1 bar. The temperature dependent standard reversible potential, E_{rev}^0, can be obtained from the literature [60]

$$E_{rev}^0 = 1.2291 - 0.0008456 \cdot (T - 298.15) \quad Equation\ SEQ\ Equation \text{¿}\ ARABIC\ 3$$

where the voltages, first two terms on right hand side of equation, are measured in V, and the temperatures in K. Under current electrolyzer testing condition, the E_{rev}^0 is calculated to be 1.168 V, with a thermoneutral voltage, E_{tn}, of 1.412 V.

Ohmic overpotential η_Ω. EIS is used to measure the high frequency resistance (HFR) representing the total electronic cell resistance R_{tot}. The ohmic overpotential, η_Ω, is therefore determined as:

$$\eta_\Omega = i * R_{tot} = i * HFR \quad Equation\ SEQ\ Equation \text{¿}\ ARABIC\ 4$$

Kinetics overpotential η_{kin}. The kinetic overpotential was extracted using a Tafel model, in which the Tafel slope b and exchange current density i_0 are the governing kinetic parameters. Assuming a non-polarizable HER, the entire kinetic overpotential of the cell is governed by OER with the Tafel slope b as 2.303*$RT/4F$ where R is the ideal gas constant, T is temperature, and F is Faraday's constant:

$$\eta_{kin} = b * \log\left(\frac{i}{i_0}\right) Equation\ SEQ\ Equation\ ¿\ ARABIC\ 5$$

Mass transport overpotential η_{mt}. The mass transport is a summary of gaseous/liquid transfer in the PTL/CL and ionic transport in the CLs. In this study, it is calculated by subtracting the reversible cell potential and kinetic and ohmic overpotentials from the measured cell potential.

Conversion Efficiency, η_{conv}. The HHV-based conversion efficiency was calculated by dividing the thermoneutral voltage (1.412 V) by the cell voltage.

$$\eta_{conv} = \frac{E_{tn}}{E_{cell}}$$

Scanning Electron Microscopy and X-ray Micro Computed Tomography

CCM surface morphology and cross-sections were imaged by a FEI Quanta FEG 250 scanning electron microscope (SEM). Ex-situ X-ray computed tomography (XCT) was conducted at the Advanced Light Source at Lawrence Berkeley National Laboratory (Beamline 8.3.2) with a PCO.Edge CCD camera, an LuAG scintillator and 20x optical lenses. The resulting images had a resolution of 0.323 μm voxel^{-1} and a horizontal field of view of 1.8 mm. The samples were prepared for tomography imaging by cutting the CCMs into ~3 mm triangular sections each having an approximately 45-degree tip and 5 mm base for mounting on the pins which are mounted on the beamline rotating stage. A multilayer monochromator was used to select the X-ray energy at 20 keV. 300 ms exposure time was used. Operando XCT and radiography imaging were conducted at Beamline 2-BM at Advanced Photon Source (APS). A multilayer monochromator was used to select 27 keV energy. The optics used were Optique 2X lens, 20 um LuAGb scintillator, resulting in 1.73 um voxel^{-1} resolution. 20 ms exposure time was used for XCT data acquisition. Radiography imaging was used to capture oxygen transport in the channels. The data was collected with the cell in-plane and through-plane configuration, using 5 ms exposure time for total time of 2 minutes per each operating condition, refer to Kulkarni et al. for the experimental arrangement[61]. Constant current holds of 1 A – 5 A and OCV was used to observe oxygen transport. For operando imaging our previous work reports the cell dimensions and design [40]. Operating temperature was 60 °C, water flow rate was 3 ml min^{-1} and active area of 1 cm^2. Images were reconstructed using TomoPy software and visualized with Dragonfly 3.6.

Oxygen content in the channel was determined using area of approximately 160 μm x 60 μm. Two such areas were selected to create representative data set of threshold values. The mean greyscale values corresponding to oxygen bubbles were collected from different points within the channel and the lowest value was the baseline for oxygen. The number of points lying above this baseline was divided by the total number of average threshold values to get the oxygen percentage in the channel. The oxygen baseline threshold was varied by ±0.5 to get error bars.

Contact area calculations were performed on interfacial area of 1 mm^2. 5 slices were selected near the interface corresponding to about 8.6 μm in length to accommodate the membrane swelling into the PTL during operation. The catalyst was thresholded within these slices and a Z-project was done to superimpose it into one single slice. The area fraction of the catalyst slice was calculated and divided by the area fraction of the PTL slice at the interface to obtain the triple phase contact area (TPCA%). Three such representative areas were selected randomly and the TPCA% was calculated at each one to get error bars.

Author Contributions

Z.T., X.P. and N.D. conceived the idea and designed the experiments. N.D., A.W., and C.H. obtained funding to support the work and provided experimental design guidance and direction, Z.T. and X.P. carried out the electrochemical measurements and analysis. D.K. and I.Z. performed the synchrotron X-ray tomography experiments and data analysis. Z.T., X.P. and N.D. wrote the manuscript and all authors edited the manuscript.

Acknowledgements and Funding

This material is based upon work supported by the U.S. Department of Energy, Office of Science, Office of Workforce Development for Teachers and Scientists, Office of Science Graduate Student Research (SCGSR) program. The SCGSR program is administered by the Oak Ridge Institute for Science and Education (ORISE) for the DOE. ORISE is managed by ORAU under contract number DE-SC0014664. All opinions expressed in this paper are the author's and do not necessarily reflect the policies and views of DOE, ORAU, or ORISE.

The micro X-ray CT experiments used beamline 8.3.2 of the Advanced Light Source, which is a DOE Office of Science User Facility under contract no. DE-AC02-05CH11231. We thank Dr. Dula Parkinson for beamline support. 3D X-ray tomography images for this paper were generated using Dragonfly software, Version 3.6. Object Research Systems (ORS) Inc, Montreal, Canada, 2018; software available at http://www.theobjects.com/dragonfly. This research used resources of the Advanced Photon Source, a U.S. Department of Energy (DOE) Office of Science User Facility operated for the DOE Office of Science by Argonne National Laboratory under Contract No. DE-AC02-06CH11357. We thank Dr. Francesco DeCarlo and Mr. Pavel Shevchenko for the beamtime support at beamline 2- BM at APS.

Supporting Information

Additional characterization, more detailed XCT and radiography images, mass and geometric area averaged overpotential breakdowns, TKK catalyst characterization.

References

(1) Lazard. *Lazard's Levelized Cost of Energy Analysis — Version 12.0*; 2018.

(2) International Energy Agency. *Global Energy and CO2 Status Report*; Paris, 2019.

(3) Bosetti, V.; Longden, T. Light Duty Vehicle Transportation and Global Climate Policy: The Importance of Electric Drive Vehicles. *Energy Policy* **2013**, *58* (July 2011), 209–219. https://doi.org/10.1016/j.enpol.2013.03.008.

(4) Schmidt, O.; Melchior, S.; Hawkes, A.; Staffell, I. Projecting the Future Levelized Cost of Electricity Storage Technologies. *Joule* **2019**, *3* (1), 81–100. https://doi.org/10.1016/j.joule.2018.12.008.

(5) Popovski, E.; Aydemir, A.; Fleiter, T.; Bellstädt, D.; Büchele, R.; Steinbach, J. The Role and Costs of Large-Scale Heat Pumps in Decarbonising Existing District Heating Networks – A Case Study for the City of Herten in Germany. *Energy* **2019**, *180*, 918–933. https://doi.org/10.1016/j.energy.2019.05.122.

(6) Davis, S. J.; Lewis, N. S.; Shaner, M.; Aggarwal, S.; Arent, D.; Azevedo, I. L.; Benson, S. M.; Bradley, T.; Brouwer, J.; Chiang, Y. M.; Clack, C. T. M.; Cohen, A.; Doig, S.; Edmonds, J.; Fennell, P.; Field, C. B.; Hannegan, B.; Hodge, B. M.; Hoffert, M. I.; Ingersoll, E.; Jaramillo, P.; Lackner, K. S.; Mach, K. J.; Mastrandrea, M.; Ogden, J.; Peterson, P. F.; Sanchez, D. L.; Sperling, D.; Stagner, J.; Trancik, J. E.; Yang, C. J.; Caldeira, K. Net-Zero Emissions Energy Systems. *Science (80-.).* **2018**, *360* (6396). https://doi.org/10.1126/science.aas9793.

(7) Mac Kinnon, M. A.; Brouwer, J.; Samuelsen, S. The Role of Natural Gas and Its Infrastructure in Mitigating Greenhouse Gas Emissions, Improving Regional Air Quality, and Renewable Resource Integration. *Prog. Energy Combust. Sci.* **2018**, *64*, 62–92. https://doi.org/10.1016/j.pecs.2017.10.002.

(8) Çabukoglu, E.; Georges, G.; Küng, L.; Pareschi, G.; Boulouchos, K. Fuel Cell Electric Vehicles: An Option to Decarbonize Heavy-Duty Transport? Results from a Swiss Case-Study. *Transp. Res. Part D Transp. Environ.* **2019**, *70* (March), 35–48.

https://doi.org/10.1016/j.trd.2019.03.004.

(9) Staffell, I.; Scamman, D.; Velazquez Abad, A.; Balcombe, P.; Dodds, P. E.; Ekins, P.; Shah, N.; Ward, K. R. The Role of Hydrogen and Fuel Cells in the Global Energy System. *Energy Environ. Sci.* **2019**, *12* (2), 463–491. https://doi.org/10.1039/c8ee01157e.

(10) Ayers, K.; Danilovic, N.; Ouimet, R.; Carmo, M.; Pivovar, B.; Bornstein, M. Perspectives on Low-Temperature Electrolysis and Potential for Renewable Hydrogen at Scale. *Annu. Rev. Chem. Biomol. Eng.* **2019**, *10* (1), 219–239. https://doi.org/10.1146/annurev-chembioeng-060718-030241.

(11) Fawcett, A. A.; Iyer, G. C.; Clarke, L. E.; Edmonds, J. A.; Hultman, N. E.; McJeon, H. C.; Rogelj, J.; Schuler, R.; Alsalam, J.; Asrar, G. R.; Creason, J.; Jeong, M.; McFarland, J.; Mundra, A.; Shi, W. Can Paris Pledges Avert Severe Climate Change? *Science (80-.).* **2015**, *350* (6265), 1168–1169. https://doi.org/10.1126/science.aad5761.

(12) Guerra, O. J.; Eichman, J.; Kurtz, J.; Hodge, B.-M. Cost Competitiveness of Electrolytic Hydrogen. *Joule* **2019**, 1–19. https://doi.org/10.1016/j.joule.2019.07.006.

(13) Parra, D.; Zhang, X.; Bauer, C.; Patel, M. K. An Integrated Techno-Economic and Life Cycle Environmental Assessment of Power-to-Gas Systems. *Appl. Energy* **2017**, *193*, 440–454. https://doi.org/10.1016/j.apenergy.2017.02.063.

(14) Pivovar, B.; Rustagi, N.; Satyapal, S. Hydrogen at Scale (H2@Scale) Key to a Clean, Economic, and Sustainable Energy System By. *The Electrochem. Soc. Interface* **2018**, *27*, 47–52.

(15) Wulf, C.; Linßen, J.; Zapp, P. Review of Power-to-Gas Projects in Europe. *Energy Procedia* **2018**, *155*, 367–378. https://doi.org/10.1016/j.egypro.2018.11.041.

(16) Public Utility District No. 1 of Douglas County. Bid Document No. 19-23-D, Supply and Deliver Hydrogen Electrolyzer Equipement. East Wenatchee, WA 2019.

(17) Ayers, K. E.; Renner, J. N.; Danilovic, N.; Wang, J. X.; Zhang, Y.; Maric, R.; Yu, H. Pathways to Ultra-Low Platinum Group Metal Catalyst Loading in Proton Exchange Membrane Electrolyzers. *Catal. Today* **2016**, *262*, 121–132.

https://doi.org/10.1016/j.cattod.2015.10.019.

(18) Yager, T. R. *2015 Minerals Yearbook The Mineral Industry of South Africa*; 2019.

(19) Yager, T. R. *2015 Minerals Yearbook The Mineral Industry of Zimbabwe*; 2019.

(20) Government of Canada. Platnium Facts https://www.nrcan.gc.ca/our-natural-resources/minerals-mining/minerals-metals-facts/platinum-facts/20520#L2.

(21) United States Geological Survey National Minerals Information Center. Platinum-Group Metals Statistics and Information https://www.usgs.gov/centers/nmic/platinum-group-metals-statistics-and-information.

(22) Babic, U.; Suermann, M.; Büchi, F. N.; Gubler, L.; Schmidt, T. J. Critical Review—Identifying Critical Gaps for Polymer Electrolyte Water Electrolysis Development. *J. Electrochem. Soc.* **2017**, *164* (4), F387–F399. https://doi.org/10.1149/2.1441704jes.

(23) International Energy Agency. Total Global Primary Energy Supply https://www.iea.org/data-and-statistics?country=WORLD&fuel=Energy supply&indicator=Total primary energy supply (TPES) by source (accessed Jun 16, 2020).

(24) Rozain, C.; Mayousse, E.; Guillet, N.; Millet, P. Influence of Iridium Oxide Loadings on the Performance of PEM Water Electrolysis Cells: Part II - Advanced Oxygen Electrodes. *Appl. Catal. B Environ.* **2016**, *182*, 123–131. https://doi.org/10.1016/j.apcatb.2015.09.011.

(25) Slavcheva, E.; Radev, I.; Bliznakov, S.; Topalov, G.; Andreev, P.; Budevski, E. Sputtered Iridium Oxide Films as Electrocatalysts for Water Splitting via PEM Electrolysis. *Electrochim. Acta* **2007**, *52* (12), 3889–3894. https://doi.org/10.1016/j.electacta.2006.11.005.

(26) Lewinski, K. A.; Van Der Vliet, D.; Luopa, S. M. NSTF Advances for PEM Electrolysis - The Effect of Alloying on Activity of NSTF Electrolyzer Catalysts and Performance of NSTF Based PEM Electrolyzers. *ECS Trans.* **2015**, *69* (17), 893–917. https://doi.org/10.1149/06917.0893ecst.

(27) Bernt, M.; Siebel, A.; Gasteiger, H. A. Analysis of Voltage Losses in PEM Water Electrolyzers with Low Platinum Group Metal Loadings. *J. Electrochem. Soc.* **2018**, *165* (5), F305–F314. https://doi.org/10.1103/PhysRevA.66.042103.

(28) Vincent, I.; Bessarabov, D. Low Cost Hydrogen Production by Anion Exchange Membrane Electrolysis : A Review. *Renew. Sustain. Energy Rev.* **2018**, *81* (May 2017), 1690–1704. https://doi.org/10.1016/j.rser.2017.05.258.

(29) Ayers, K. The Potential of Proton Exchange Membrane Based Electrolysis Technology. *Curr. Opin. Electrochem.* **2019**, *18*, 9–15. https://doi.org/10.1016/j.coelec.2019.08.008.

(30) Babic, U.; Schmidt, T. J.; Gubler, L. Communication—Contribution of Catalyst Layer Proton Transport Resistance to Voltage Loss in Polymer Electrolyte Water Electrolyzers. *J. Electrochem. Soc.* **2018**, *165* (15), J3016–J3018. https://doi.org/10.1149/2.0031815jes.

(31) Lopata, J.; Kang, Z.; Young, J.; Bender, G.; Weidner, J. W.; Shimpalee, S.; Shimpalee, S.; Professor, R. Effects of the Transport/Catalyst Layer Interface and Catalyst Loading on Mass and Charge Transport Phenomena in Polymer Electrolyte Membrane Water Electrolysis Devices. *J. Electrochem. Soc.* **2020**, *167* (6), 64507. https://doi.org/10.1149/1945-7111/ab7f87.

(32) Bender, G.; Carmo, M.; Smolinka, T.; Gago, A.; Danilovic, N.; Mueller, M.; Ganci, F.; Fallisch, A.; Lettenmeier, P.; Friedrich, K. A.; Ayers, K.; Pivovar, B.; Mergel, J.; Stolten, D. Initial Approaches in Benchmarking and Round Robin Testing for Proton Exchange Membrane Water Electrolyzers. *Int. J. Hydrogen Energy* **2019**, *44* (18), 9174–9187. https://doi.org/10.1016/j.ijhydene.2019.02.074.

(33) Mo, J.; Kang, Z.; Retterer, S. T.; Cullen, D. A.; Toops, T. J.; Green, J. B.; Mench, M. M.; Zhang, F. Y. Discovery of True Electrochemical Reactions for Ultrahigh Catalyst Mass Activity in Water Splitting. *Sci. Adv.* **2016**, *2* (11). https://doi.org/10.1126/sciadv.1600690.

(34) Schuler, T.; Kimura, T.; Schmidt, T. J.; Buchi, F. N. Towards a Generic Understanding of Oxygen Evolution Reaction Kinetics in Polymer Electrolyte Water Electrolysis. *Energy Environ. Sci.* **2020**. https://doi.org/10.1039/d0ee00673d.

(35) Schuler, T.; Ciccone, J. M.; Krentscher, B.; Marone, F.; Peter, C.; Schmidt, T. J.; Büchi, F. N. Hierarchically Structured Porous Transport Layers for Polymer Electrolyte Water Electrolysis. *Adv. Energy Mater.* **2019**, 1903216–1903228. https://doi.org/10.1002/aenm.201903216.

(36) Suermann, M.; Schmidt, T. J.; Buchi, F. N. Investigation of Mass Transport Losses in Polymer Electrolyte Electrolysis Cells. In *ECS Transactions*; 2015; Vol. 69, pp 1141–1148. https://doi.org/10.1149/06917.1141ecst.

(37) Matsumoto, Y.; Sato, E. Electrocatalytic Properties of Tranistion Metal Oxides for Oxygen Evolution Reaction. *Mater. Chem. Phys.* **1986**, *14*, 397–426.

(38) Babic, U.; Nilsson, E.; Patru, A.; Schmidt, T. J.; Gubler, L. Proton Transport in Catalyst Layers of a Polymer Electrolyte Water Electrolyzer: Effect of the Anode Catalyst Loading. *J. Electrochem. Soc.* **2019**, *166* (4), F214–F220. https://doi.org/10.1149/2.0341904jes.

(39) Zhou, J.; Johansen, H.; Danilovic, N.; Zenyuk, I.; Weber, A. Z. Multiscale Modeling of Multiphase Transport in PEM Water Electrolyzer. In *ECS Meeting Abstracts*; 2019.

(40) Leonard, E.; Shum, A. D.; Danilovic, N.; Capuano, C.; Ayers, K. E.; Pant, L. M.; Weber, A. Z.; Xiao, X.; Parkinson, D. Y.; Zenyuk, I. V. Interfacial Analysis of a PEM Electrolyzer Using X-Ray Computed Tomography. *Sustain. Energy Fuels* **2020**. https://doi.org/10.1039/c9se00364a.

(41) Grigoriev, S. A.; Millet, P.; Volobuev, S. A.; Fateev, V. N. Optimization of Porous Current Collectors for PEM Water Electrolysers. *Int. J. Hydrogen Energy* **2009**, *34* (11), 4968–4973. https://doi.org/10.1016/j.ijhydene.2008.11.056.

(42) Ito, H.; Maeda, T.; Nakano, A.; Kato, A.; Yoshida, T. Influence of Pore Structural Properties of Current Collectors on the Performance of Proton Exchange Membrane Electrolyzer. *Electrochim. Acta* **2013**, *100*, 242–248. https://doi.org/10.1016/j.electacta.2012.05.068.

(43) Ito, H.; Maeda, T.; Nakano, A.; Hwang, C. M.; Ishida, M.; Kato, A.; Yoshida, T. Experimental Study on Porous Current Collectors of PEM Electrolyzers. *Int. J. Hydrogen*

Energy **2012**, *37* (9), 7418–7428. https://doi.org/10.1016/j.ijhydene.2012.01.095.

(44) Suermann, M.; Takanohashi, K.; Lamibrac, A.; Schmidt, T. J.; Büchi, F. N. Influence of Operating Conditions and Material Properties on the Mass Transport Losses of Polymer Electrolyte Water Electrolysis. *J. Electrochem. Soc.* **2017**, *164* (9), F973–F980. https://doi.org/10.1149/2.13517109jes.

(45) Newman, J.; Thomas-Alyea, K. *Electrochemical Systems*, Third.; Wiley-Interscience, 2004.

(46) Zhao, S.; Yu, H.; Maric, R.; Danilovic, N.; Capuano, C. B.; Ayers, K. E.; Mustain, W. E. Calculating the Electrochemically Active Surface Area of Iridium Oxide in Operating Proton Exchange Membrane Electrolyzers. *J. Electrochem. Soc.* **2015**. https://doi.org/10.1149/2.0211512jes.

(47) Mayyas, A.; Ruth, M.; Pivovar, B.; Bender, G.; Wipke, K. *Manufacturing Cost Analysis for Proton Exchange Membrane Water Electrolyzers*; 2019.

(48) International Energy Agency. Key World Energy Statistics - Total final consumption https://www.iea.org/statistics/kwes/consumption/ (accessed Jan 11, 2019).

(49) Siracusano, S.; Baglio, V.; Van Dijk, N.; Merlo, L.; Aricò, A. S. Enhanced Performance and Durability of Low Catalyst Loading PEM Water Electrolyser Based on a Short-Side Chain Perfluorosulfonic Ionomer. *Appl. Energy* **2017**, *192*, 477–489. https://doi.org/10.1016/j.apenergy.2016.09.011.

(50) Lee, B. S.; Ahn, S. H.; Park, H. Y.; Choi, I.; Yoo, S. J.; Kim, H. J.; Henkensmeier, D.; Kim, J. Y.; Park, S.; Nam, S. W.; Lee, K. Y.; Jang, J. H. Development of Electrodeposited IrO2 Electrodes as Anodes in Polymer Electrolyte Membrane Water Electrolysis. *Appl. Catal. B Environ.* **2015**, *179*, 285–291. https://doi.org/10.1016/j.apcatb.2015.05.027.

(51) Lee, B. S.; Park, H. Y.; Choi, I.; Cho, M. K.; Kim, H. J.; Yoo, S. J.; Henkensmeier, D.; Kim, J. Y.; Nam, S. W.; Park, S.; Lee, K. Y.; Jang, J. H. Polarization Characteristics of a Low Catalyst Loading PEM Water Electrolyzer Operating at Elevated Temperature. *J. Power Sources* **2016**, *309*, 127–134. https://doi.org/10.1016/j.jpowsour.2015.12.139.

(52) Su, H.; Bladergroen, B. J.; Linkov, V.; Pasupathi, S.; Ji, S. Study of Catalyst Sprayed Membrane under Irradiation Method to Prepare High Performance Membrane Electrode Assemblies for Solid Polymer Electrolyte Water Electrolysis. *Int. J. Hydrogen Energy* **2011**, *36* (23), 15081–15088. https://doi.org/10.1016/j.ijhydene.2011.08.057.

(53) Ma, L.; Sui, S.; Zhai, Y. Investigations on High Performance Proton Exchange Membrane Water Electrolyzer. *Int. J. Hydrogen Energy* **2009**, *34* (2), 678–684. https://doi.org/10.1016/j.ijhydene.2008.11.022.

(54) Xu, W.; Scott, K. The Effects of Ionomer Content on PEM Water Electrolyser Membrane Electrode Assembly Performance. *Int. J. Hydrogen Energy* **2010**, *35* (21), 12029–12037. https://doi.org/10.1016/j.ijhydene.2010.08.055.

(55) Su, H.; Linkov, V.; Bladergroen, B. J. Low Noble Metal Loadings for Hydrogen Production From Solid Polymer Electrolyte Water Electrolysis. *Int. J. Hydrogen Energy* **2013**, *38* (23), 9601–9608. https://doi.org/10.1016/j.ijhydene.2013.05.099.

(56) Bernt, M.; Gasteiger, H. A. Influence of Ionomer Content in IrO2/TiO2 Electrodes on PEM Water Electrolyzer Performance. *J. Electrochem. Soc.* **2016**, *163* (11), F3179–F3189. https://doi.org/10.1149/2.0231611jes.

(57) Park, J. E.; Kim, S.; Kim, O. H.; Ahn, C. Y.; Kim, M. J.; Kang, S. Y.; Jeon, T. Il; Shim, J. G.; Lee, D. W.; Lee, J. H.; Cho, Y. H.; Sung, Y. E. Ultra-Low Loading of IrO2 with an Inverse-Opal Structure in a Polymer-Exchange Membrane Water Electrolysis. *Nano Energy* **2019**, *58* (January), 158–166. https://doi.org/10.1016/j.nanoen.2019.01.043.

(58) Sapountzi, F. M.; Divane, S. C.; Papaioannou, E. I.; Souentie, S.; Vayenas, C. G. The Role of Nafion Content in Sputtered IrO2 Based Anodes for Low Temperature PEM Water Electrolysis. *J. Electroanal. Chem.* **2011**, *662* (1), 116–122. https://doi.org/10.1016/j.jelechem.2011.04.005.

(59) Hegge, F.; Lombeck, F.; Ortiz, E. C.; Bohn, L.; Holst, M. Von; Kroschel, M.; Hübner, J.; Breitwieser, M.; Strasser, P.; Vierrath, S. Efficient and Stable Low Iridium-Loaded Anodes for PEM Water Electrolysis Made Possible by Nanofiber Interlayers. *Appl. Energy Mater.* **2020**. https://doi.org/10.1021/acsaem.0c00735.

(60) Bratsch, S. G. Standard Electrode Potentials and Temperature Coefficients in Water at 298.15 K. *J. Phys. Chem. Ref. Data* **1989**. https://doi.org/10.1063/1.555839.

(61) Kulkarni, D.; Normile, S.; Connolly, L.; Zenyuk, I. Development of Low Temperature Fuel Cell Holders for Operando X-Ray Micro and Nano Computed Tomography to Visualize Water Distribution. *J. Phys. Energy* **2020**. https://doi.org/10.1088/2515-7655/abb783.

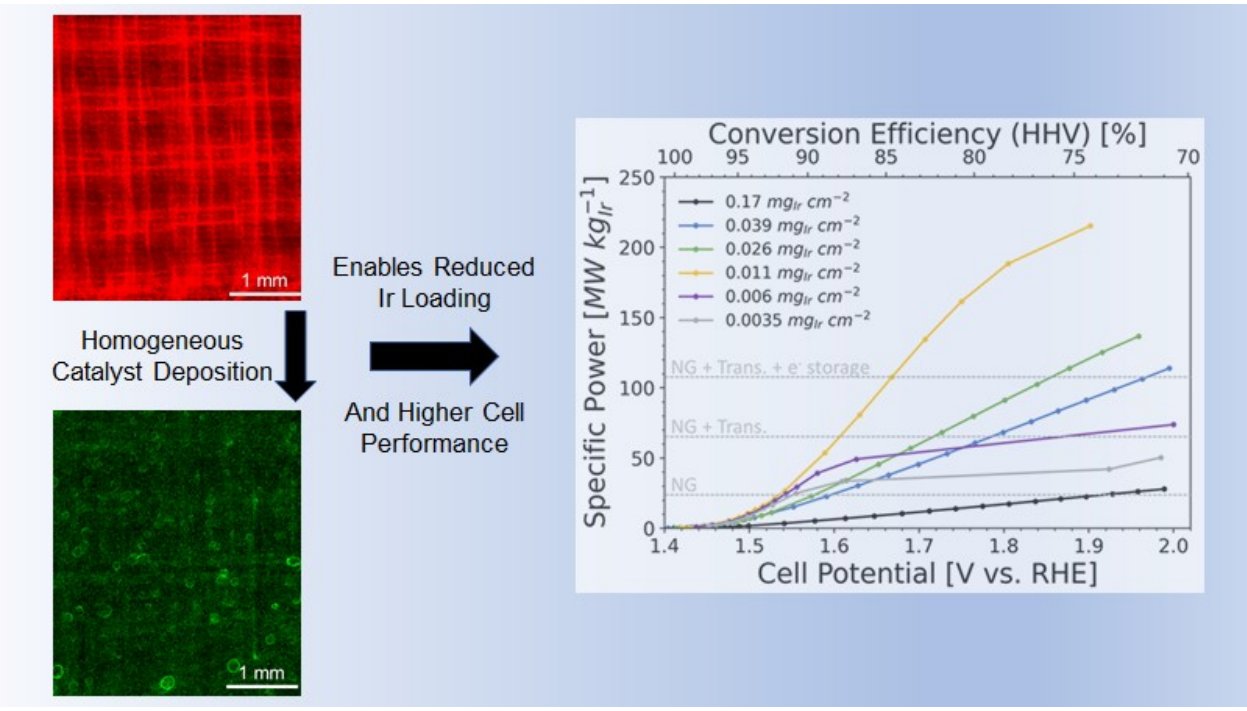
1 mm
Homogeneous
Catalyst Deposition
1 mm
Enables Reduced
Ir Loading
And Higher Cell
Performance
Conversion Efficiency (HHV) [%]
100
95
90
85
80
75
70
Specific Power [MW kg$_{Ir}^{-1}$]
250
200
150
100
50
0
0.17 mg$_{Ir}$ cm^{-2}
0.039 mg$_{Ir}$ cm^{-2}
0.026 mg$_{Ir}$ cm^{-2}
0.011 mg$_{Ir}$ cm^{-2}
0.006 mg$_{Ir}$ cm^{-2}
0.0035 mg$_{Ir}$ cm^{-2}
NG + Trans. + e⁻ storage
NG + Trans.
NG
1.4
1.5
1.6
1.7
1.8
1.9
2.0
Cell Potential [V vs. RHE]